UNIVERSIDADE FEDERAL DE SÃO CARLOS
CENTRO DE CIÊNCIAS EXATAS E DE TECNOLOGIA
PROGRAMA DE PÓS-GRADUAÇÃO EM CIÊNCIA E ENGENHARIA DE MATERIAIS

UNIVERSITÉ DU QUÉBEC À TROIS-RIVIÈRES
DOCTORAT EN SCIENCES DE L'ÉNERGIE ET DES MATÉRIAUX

DESIGN OF HIGH ENTROPY ALLOYS FOR HYDROGEN STORAGE: STUDY OF THE Mg-V-Al-Cr-Ni, Mg-Al-Ti-Mn-Nb and Ti-V-Nb-Cr SYSTEMS

Renato Belli Strozi

São Carlos
2021

UNIVERSIDADE FEDERAL DE SÃO CARLOS
CENTRO DE CIÊNCIAS EXATAS E DE TECNOLOGIA
PROGRAMA DE PÓS-GRADUAÇÃO EM CIÊNCIA E ENGENHARIA DE MATERIAIS

UNIVERSITÉ DU QUÉBEC À TROIS-RIVIÈRES
DOCTORAT EN SCIENCES DE L'ÉNERGIE ET DES MATÉRIAUX

DESIGN OF HIGH ENTROPY ALLOYS FOR HYDROGEN STORAGE: STUDY OF THE Mg-V-Al-Cr-Ni, Mg-Al-Ti-Mn-Nb and Ti-V-Nb-Cr SYSTEMS

Renato Belli Strozi

Tese apresentada ao Programa de Pós-Graduação em Ciência e Engenharia de Materiais como requisito parcial à obtenção do título de DOUTOR EM CIÊNCIA E ENGENHARIA DE MATERIAIS

Supervisor at Brazil: Prof. Dr. Daniel Rodrigo Leiva
Supervisor at Canada: Prof. Dr. Jacques Huot
Co-supervisor: Prof. Dr. Guilherme Zepon
Funding agencies: CAPES (process: 88882.332724/2019-01). NSERC-Canada. Serrapilheira Institute.

São Carlos
2021

DEDICATION

This doctoral thesis is devoted to my family, my support and inspiration, with all my love.

VITAE DO CANDIDATO

MSc. in Materials Science and Engineering at Federal University of São Carlos (2017), BSc. in Science Education with a major in Chemistry at the University of Sao Paulo (2013).

UNIVERSIDADE FEDERAL DE SÃO CARLOS

Centro de Ciências Exatas e de Tecnologia
Programa de Pós-Graduação em Ciência e Engenharia de Materiais

Folha de Aprovação

Defesa de Tese de Doutorado do candidato Renato Belli Strozi, realizada em 21/05/2021.

Comissão Julgadora:

Prof. Dr. Daniel Rodrigo Leiva (UFSCar)

Prof. Dr. Walter José Botta Filho (UFSCar)

Prof. Dr. Ricardo Floriano (UNICAMP)

Prof. Dr. Ricardo Mendes Leal Neto (IPEN)

Prof. Dr. Jacques Goyette (UQTR)

Prof. Dr. Jacques Huot (UQTR)

O presente trabalho foi realizado com apoio da Coordenação de Aperfeiçoamento de Pessoal de Nível Superior - Brasil (CAPES) - Código de Financiamento 001.
O Relatório de Defesa assinado pelos membros da Comissão Julgadora encontra-se arquivado junto ao Programa de Pós-Graduação em Ciência e Engenharia de Materiais.

ACKNOWLEDGMENT

This study was financed in part by the Coordenação de Aperfeiçoamento de Pessoal de Nível Superior – Brasil (CAPES) - Finance Code 001.

This work was funded in part by the Serrapilheira Institute (grant number Serra-1709-17362).

This work was supported in part by a Discovery Grant from the Natural Sciences and Engineering Research Council of Canada (NSERC).

I am very grateful to my supervisor in Brazil, Professor Daniel Rodrigo Leiva, for this huge opportunity as well as for his valuable advice, patience, and support, always encouraging me and saying calm and appropriate words.

I would like to thank my supervisor in Canada, Professor Jacques Huot, for welcoming me abroad. It was an amazing period in my life. I also would like to thank him for all his attention. I am grateful to him for every single discussion we had during that period, which undoubtedly contributed to making me a better researcher and human being.

Special thanks to my friend and co-supervisor, Professor Guilherme Zepon, for his hard work and resilience throughout this exciting journey. It is a huge inspiration to learn materials science from a brilliant scientist like him.

I am also deeply grateful to my dear friends for sharing with me special moments. Here, it is important to mention that I consider myself a very lucky person who has the best friends ever. Special thanks to my friends from childhood, Pinho, Lê Cardilli e Maumau and my friends of all my life, especially Hilde, Caio, and Ozzy. These friends have made my life easier, and their unrestricted support has made everything better.

Special thanks to my friends from my research group and everyday life in Brazil and Canada: Marcelo Cavallaro, Pistola, Ferrugem, Débi, Witão, Vitão Banzo, Chico, Otani, Jack, Eric, Lô, Vidilli, Diego Santana, Ricardo Petrilli, Vinicius, André Neves, Catarina Pio, Elena, Erika, Saeed, Flavio, Alexandre, Augusto, Eric, and Anthony, as well as to the LCE staff, who deserve special attention. I am glad to share this journey with such amazing people.

I would like to thank my mother, Lucia, and my grandparents, Lourdes and Christiano. They are my everything, and there are no words to express how grateful I am to them for their constant love and support.

Finally, I would like to thank my girlfriend, Daniela dos Santos, for her unwavering love and support throughout the years. She keeps inspiring and teaching me, being the best and fundamental part of my days.

ABSTRACT

The advent of high entropy alloys (HEA) has brought new opportunities and challenges to metallurgy. Due to extensive compositional field of HEAs, the possibility of controlling properties in a composition-driven approach becomes evident. However, this vast compositional field demands enormous efforts to select promising alloys for a given application. Up to now, an accurate model to effectively designing HEAs for hydrogen storage is still lacking. Thus, this thesis is dedicated to investigating the effects of the chemical composition on the structural and hydrogen storage properties of body-centered cubic (BCC) HEAs for hydrogen storage applications. Firstly, a set of lightweight HEAs of the Mg-V-Al-Cr-Ni system was produced by high-energy ball milling (HEBM). The experimental results indicate that a single-phase solid solution was only obtained for the equiatomic composition. The investigated alloys exhibited poor hydrogen storage properties. This behavior brought to light the importance of balancing hydride- and non-hydride-forming elements to tune the alloy's hydrogen affinity, specially considering the mean enthalpy of hydrogen solution of the alloying elements ($\overline{\Delta H_{\infty}}$). In a second step, a semi-empirical design method was employed to screen a single-phase BCC alloy with high hydrogen affinity from the Mg-Al-Ti-Mn-Nb system. Through the calculation of four composition-dependent parameters (φ, VEC, $\overline{\Delta H_{\infty}}$ and $\overline{\Delta H_f^o}$), the $Mg_{12}Al_{11}Ti_{33}Mn_{11}Nb_{33}$ alloy was designed. When produced by HEBM, this alloy exhibited a single-phase BCC structure and interesting hydrogen storage properties, indicating that the design approach can be successfully applied to find interesting compositional regions for a multicomponent system, decreasing the number of experiments needed to find alloys with appropriate properties for hydrogen storage. In the third part of this study, the effects of adding a non-hydride-forming element in a multicomponent system composed only of hydride-forming elements was investigated. The CALPHAD method was applied to find a suitable alloy system. The $(TiVNb)_{100-x}Cr_x$ alloy system was selected, with x = 15, 25, and 35 at.%. In this range of composition, the CALPHAD method indicates the formation of single-phase BCC during solidification for the three alloys, which was confirmed experimentally. The hydrogen storage performance was evaluated, and it was verified that increasing

the Cr/(TiVNb) ratio leads to significant increase in the equilibrium plateau pressure of the $(TiVNb)_{100-x}Cr_x$ alloys, without significant loss of maximum hydrogen storage capacity. It was demonstrated that the proportion of a non-hydride forming element can be used to tune the hydrogen storage properties of the HEAs.

RESUMO

DESIGN DE LIGAS DE ALTA ENTROPIA PARA ARMAZENAMENTO DE HIDROGÊNIO: ESTUDO DOS SISTEMAS Mg-V-Al-Cr-Ni, Mg-Al-Ti-Mn-Nb e Ti-V-Nb-Cr

O advento das ligas de alta entropia (do inglês, HEA) vem abrindo novos caminhos na metalurgia. Devido ao extenso campo composicional dessa nova classe de ligas, a possibilidade de controlar propriedades em uma abordagem baseada em composição parece evidente. No entanto, este vasto campo composicional exige enormes esforços na seleção de ligas promissoras para uma determinada aplicação. Atualmente, ainda não existem relatos de trabalhos dedicados ao design de HEAs para armazenamento de hidrogênio. Assim, esta tese é dedicada a investigar os efeitos da composição química nas propriedades estruturais e de armazenamento de hidrogênio de HEAs de estrutura cúbicas centrados no corpo (do inglês, BCC), desenvolvidas para aplicações de armazenamento de hidrogênio. Inicialmente, um conjunto de ligas de alta entropia do sistema Mg-V-Al-Cr-Ni foi produzido por moagem de alta energia (do inglês, HEBM). Os resultados experimentais indicaram que uma solução sólida monofásica foi obtida apenas para a composição quinaria e equiatômica. Além disso, as ligas investigadas exibiram propriedades de armazenamento de hidrogênio pobres. Este comportamento trouxe à luz a importância do balanço da fração de elementos formadores e não formadores de hidretos simples na composição de ligas BCCs, especialmente considerando a entalpia média da solução de hidrogênio dos elementos de liga ($\overline{\Delta \mathrm{H}_{\infty}}$). Em uma segunda etapa, visando obter uma liga BCC monofásica com alta afinidade ao hidrogênio, um método de projeto semiempírico foi empregado na triagem de ligas do sistema Mg-Al-Ti-Mn-Nb. Através do cálculo de quatro parâmetros dependentes da composição (φ, *VEC*, $\overline{\Delta H_{\infty}}$ and $\overline{\Delta H_{\mathrm{f}}^{0}}$), foi proposta a liga $Mg_{12}Al_{11}Ti_{33}Mn_{11}Nb_{33}$. A composição selecionada foi então processada por HEBM. Os resultados experimentais mostraram a formação de uma liga monofásica BCC com propriedades interessantes de armazenamento de hidrogênio. Esses resultados indicam sucesso na abordagem de design, diminuindo consideravelmente o

número de experimentos necessários para encontrar campos composicionais de interesse. Na terceira parte deste estudo, foram investigados os efeitos da adição de um elemento não formador de hidreto em um sistema multicomponente composto apenas por elementos formadores de hidretos. Inicialmente, o método CALPHAD foi aplicado para encontrar um sistema adequado, onde ligas do sistema $(TiVNb)_{100-x}Cr_x$ foram propostas (x = 15, 25, and 35 at.%). Nessa faixa de composição, o método CALPHAD indica a formação de ligas monofásicas BCCs, o que foi confirmado experimentalmente. As propriedades de armazenamento de hidrogênio foram avaliadas, e verificou-se que o aumento da relação Cr/(TiVNb) leva ao aumento da pressão de equilíbrio destas ligas, contudo, sem perda significativa da capacidade máxima de armazenamento de hidrogênio. Desta maneira, foi demonstrado que a proporção de um elemento não formador de hidreto pode ser usada para ajustar as propriedades de armazenamento de hidrogênio de HEAs.

RÉSUMÉ

CONCEPTION D'ALLIAGES À HAUTE ENTROPIE POUR LE STOCKAGE D'HYDROGÈNE : ÉTUDE DES SYSTÈMES Mg-V-Al-Cr-Ni, Mg-Al-Ti-Mn-Nb et Ti-V-Nb-Cr

L'avènement des alliages à haute entropie (de l'anglais, HEA) a apporté de nouvelles opportunités et de nouveaux défis à la métallurgie. En raison du vaste champ de composition de cette nouvelle classe d'alliages, la possibilité de contrôler les propriétés dans une approche basée sur la composition semble évidente. Cependant, ce large domaine de composition nécessite d'énormes efforts dans la sélection d'alliages prometteurs pour une application donnée. Actuellement, il n'y a pas de rapports de travaux consacrés à la conception des HEA pour le stockage de l'hydrogène. Ainsi, cette thèse étudie les effets de la composition chimique sur les propriétés structurelles et de stockage d'hydrogène des HEA à structure cubique centrée (de l'anglais, BCC), développés pour des applications de stockage d'hydrogène. Initialement, un ensemble de HEAs du système Mg-V-Al-Cr-Ni a été produit par broyage à haute énergie (de l'anglais, HEBM). Les résultats expérimentaux ont indiqué qu'une solution solide monophasique n'a été obtenue que pour la composition quinaire et équiatomique. De plus, les alliages étudiés présentaient de mauvaises propriétés de stockage d'hydrogène. Ce comportement a mis en évidence l'importance de l'équilibre de la fraction des éléments formant et non formant des hydrures simples dans la composition des alliages BCC, notamment compte tenu de l'enthalpie moyenne de la solution d'hydrogène des éléments d'alliage ($\overline{\Delta H_{\infty}}$). Dans une seconde étape, visant à obtenir un alliage BCC monophasé à forte affinité pour l'hydrogène, une méthode de conception semi-empirique a été utilisée pour cribler les alliages du système Mg-Al-Ti-Mn-Nb. Grâce au calcul de quatre paramètres dépendants de la composition (φ, *VEC*, $\overline{\Delta H_{\infty}}$ et $\overline{\Delta H_f^o}$), l'alliage $Mg_{12}Al_{11}Ti_{33}Mn_{11}Nb_{33}$ a été proposé. La composition sélectionnée a été produite par HEBM. Les résultats expérimentaux ont montré la formation d'un alliage BCC monophasique avec des propriétés intéressantes de stockage d'hydrogène. Ces résultats indiquent le succès de l'approche de conception, réduisant

considérablement le nombre d'expériences nécessaires pour trouver des champs compositionnels d'intérêt. Dans la troisième partie de cette étude, les effets de l'ajout d'un élément non formateur d'hydrure à un système à plusieurs composants composé uniquement d'éléments formateurs d'hydrure ont été étudiés. Dans un premier temps, la méthode CALPHAD a été appliquée pour trouver un système approprié, où des alliages du système $(TiVNb)_{100-x}Cr_x$ ont été proposés (x = 15, 25, and 35 at.%). Dans cette gamme de composition, la méthode CALPHAD indique la formation d'alliages BCCs monophasiques, ce qui a été confirmé expérimentalement. Les propriétés de stockage d'hydrogène ont été évaluées, et il a été constaté que l'augmentation du rapport Cr/(TiVNb) conduit à une augmentation de la pression d'équilibre de ces alliages, cependant, sans perte significative de la capacité maximale de stockage d'hydrogène. De cette manière, il a été démontré que la proportion d'un élément non formateur d'hydrure peut être utilisée pour ajuster les propriétés de stockage d'hydrogène des HEA.

PUBLICATIONS

R.B. Strozi, D.R. Leiva, G. Zepon, W.J. Botta, J. Huot.; Effects of the chromium content in $(TiVNb)_{100-x}Cr_x$ body-centered cubic high entropy alloys designed for hydrogen storage applications. **Energies**. 14 (2021), 3068. doi.org/10.3390/en14113068.

R.B. Strozi, D.R. Leiva, J. Huot, W.J. Botta, G. Zepon.; An approach to design single BCC Mg-containing high entropy alloys for hydrogen storage applications. **Int. J. Hydrogen Energy**. doi.org/10.1016/j.ijhydene.2021.05.087.

R.B. Strozi, D.R. Leiva, J. Huot, W.J. Botta, G. Zepon, Synthesis and hydrogen storage behavior of Mg–V–Al–Cr–Ni high entropy alloys, **Int. J. Hydrogen Energy**. 46 (2020) 2351–2361. doi:10.1016/j.ijhydene.2020.10.106.

INDEX

Page

TABLE INDEX

FIGURE INDEX

Page

xx

1 INTRODUCTION

For a long time, the primary energy supply framework is based on the earth's fossil fuel sources. However, recent scientific advances are screening a new scenario. Nowadays, intensive research efforts to develop technologies to leverage renewable and non-polluting energy sources are in the course, and a complete energetic transition to a most environmentally friendly, efficient, and reliable energy supply seems irreversible.

A successful energy transition demands fossil fuel power plants' replacement by renewable energy sources such as solar, wind, and hydropower plants. In this scenario, hydrogen as an energy vector can play an important role to decouple electricity production and utilization. For instance, hydrogen can be produced from water by electrolyze that demand electricity. This electricity can be produced by renewable energy sources, while its consumption can be carried out in fuel cells to generate electricity for the end-users, closing an environmentally cleaner energy cycle. However, the wide use of hydrogen in our society is limited due to its storage challenges. Conventional ways of storing hydrogen such as liquid and gaseous have some limitations in terms of temperature and high operating pressure. The high volumetric H storage capacity of metal hydrides makes them attractive compared to traditional hydrogen storage methods [1]. Metal hydrides can be used in many ways, such as in grid-connected renewable energy systems, underwater applications (e.g., fuel-cell submarines), and heavy-duty utility vehicles [2]. Additionally, hydrogen compression technology [3] and thermal energy storage [5] are good examples of complementary technologies with metal hydrides.

Metal hydrides are compounds in which hydrogen interacts with a host metal and the selection of a proper alloy (host metal) is crucial to control the hydride properties such as heat of reaction, hydrogenation/dehydrogenation kinetics and hydrogen storage capacity [4]. Numerous researchers aim to improve metal hydrides properties, and in the last few years, a new class of materials has attracted attention: the high entropy alloys (HEAs).

HEAs were firstly reported in 2004 [5,6] and the motivation was to investigate an unexplored multi-composition space as close as possible to equiatomic compositions. HEAs differ from conventional alloys, e.g., Fe, Al, Ti, or Mg-based alloys, due to the absence of a principal element. Also known as multiprincipal element alloys (MPEAs), the

term HEA's rationalization is based on the high number of principal elements, which increases the configurational entropy of mixing of a random solid solution. This can create a favorable condition to stabilize single-phase disordered solid solutions rather than multiphase structures (with intermetallic compounds) at high temperatures [6,7]. Different approaches can be used to find the compositional regions of multicomponent systems that can form single-phase alloys. Probably, the most used for this purpose is the Calculation of Phase Diagrams (CALPHAD) method. Also, the adoption of semi-empirical models to evaluate an alloy's tendency to form a single-phase solid solution over intermetallic compounds or multiphase structures [8–12].

HEA-based metal hydrides are considered promising candidates for solid-state hydrogen storage. The vast composition field allows to find alloys with different properties, and through alloy design techniques, it is possible to develop alloys with optimized and controlled properties. For example, HEAs with Laves-type phases, such as TiZrCrMnFeNi [13], CoFeMnTiVZr [14] and ZrTiVNiCrFe [15], can absorb hydrogen at room temperature forming hydrides with a hydrogen-to-metal ratio (H/M) of about 1. Higher hydrogen uptake can be reached using refractory body-centered cubic (BCC) HEAs such as TiZrNbHfTa [16,17], HfNbTiVZr [18,19] and TiVZrNbTa [20]. These alloys absorb hydrogen by forming hydrides with H/M~2, making them promising candidates for competitive hydrogen storage.

To the best of our knowledge, a useful methodology to screen different systems in the endless compositional space of HEAs to design alloys with attractive hydrogen storage properties has not been reported so far. Therefore, this thesis proposes studying the structure and hydrogen storage properties of HEAs designed for hydrogen storage applications, focusing on BCC alloys. Three different alloy systems were studied: Mg-Al-V-Cr-Ni, Mg-Al-Mn-Ti-Nb, and Ti-V-Nb-Cr. For each alloy system, a specific design approach was used.

2 OBJECTIVES

This doctoral thesis investigates the effects of the composition on the structural and hydrogen storage properties of BCC HEAs for hydrogen storage applications. For this purpose, three alloy systems were studied, namely, Mg-V-Al-Cr-Ni, Mg-Al-Mn-Ti-Nb, and Ti-V-Nb-Cr. For each system, a specific designing method and processing route were employed. The synthesized alloys were characterized in terms of micro and nanostructure, and then their hydrogen storage properties were evaluated. The ultimate goal was to understand how the chemical composition affects both structure and hydrogen storage properties, and how this knowledge can contribute to designing appropriate high entropy alloys for hydrogen storage.

3 LITERATURE REVIEW

3.1 High Entropy Alloys Design

HEAs began to be explored in the early 2000s. HEA is usually defined as an alloy having at least five principal elements distributed in a compositional range between 5 and 35 at.% [6,21], increasing the configurational entropy of mixing of a random solid solution, which is given by equation 1 [22].

$$\Delta S_c = -R \sum_{i=1}^{n} x_i \cdot \ln x_i \quad (1)$$

where i, x_i and R are, respectively, the alloy elements, the atomic fraction of the i^{th} element and the ideal gas constant.

From a thermodynamic point of view, the study of possible phases present in an alloy (the system) is given by comparing their stability. The relative stability for each phase in a system is determined by their Gibbs Free Energy (ΔG). Thus, the phase's stability results from a competition between all possible phases concerning their Gibbs free energy, where the phase with the most negative ΔG values tend to stabilize. The Gibbs free energy of a system is defined by equation 2:

$$G = H - TS \quad (2)$$

where H is the enthalpy, T is the absolute temperature, and S the system's entropy.

As can be seen in Equation 1, the configurational entropy's magnitude is closely associated with the number of elements. Increasing the number of principal elements increases the system's configurational entropy, achieving maximum values for equiatomic compositions. Thus, when observing the strong influence of the Gibbs Free Energy's entropic component, it is intuitive to state that in HEAs, a disordered solid solution phase tends to form because of the high configurational entropy of such phase. This phenomenon is defined as the high entropy effect. However, the analysis of the relative magnitude of thermodynamic quantities associated with the Gibbs Free Energy of a system must be conducted with caution. Usually, the high entropy effect by itself is not sufficient to avoid the formation of intermetallic or second phases in HEAs [23]. To assess

the competition of ΔG between the phases, it is necessary to consider all the terms that compose the Free Energy function, such as the enthalpy of mixing (H_{ss}) and the total entropy of mixing (S_{ss}), which considers other portions of entropy besides the configurational entropy of mixing of random solid solutions and compare them with the enthalpy (H_{im}) and entropy (S_{im}) of possible intermetallic phases. The comparison between the Gibbs Free Energy curves for the different phases can lead to more than a minimum point for a given temperature, indicating that two or more phases with different compositions from each other can coexist. Therefore, it is not uncommon to observe more than one phase in HEAs.

For HEA design, to select compositions that form single-phase solid solutions, it is necessary to introduce techniques and parameters beyond the high entropy effect. Due to the broad spectrum of composition, experimental determination of HEAs phase diagram is impractical. A huge number of experiments to obtain input data are necessary. Consequently, for these alloys, thermodynamic simulations based only on empirical parameters are invaluable. Therefore, designing and studying new multicomponent alloys is of great interest, and probably, the most powerful tool to assist HEAs' design is the Calculation of Phase Diagrams (CALPHAD) method.

3.1.1 CALPHAD METHOD

The CALPHAD method was proposed by Kaufman and Ansara and provides reasonable predictions about phase stability in a broad composition universe [24]. The method consists of obtaining Gibbs free energy functions from all phases in an alloy system. These curves are described as a function of state variables, such as pressure, temperature, composition, and empirical parameters (input data). The conceptual relationship between phase diagrams and free energy is well known. However, the use of the CALPHAD method enabled a significant reduction in the number of experiments.

The fundamental principle of the CALPHAD approach is to perform Gibbs free energy minimization of all possible phases of the system. In general, for the thermodynamic calculations of each given α phase, the program uses the sum of three

main terms: the reference term, one ideal mixing term, and an excess term. Thus, the free energy for a specific phase can be calculated according to equation 3.

$$G_{\propto} = {}^{ref}G_{\propto} + {}^{id}G_{\propto} + {}^{ex}G_{\propto} \quad (3)$$

For better understanding, consider the case of completely random mixing of atoms (substitutional random solutions), where only one sub-lattice is needed for thermodynamic description. In this case, one phase shows complete solubility between two elements, and G can be described according to equation 4.

$$G_m = \sum_i x_i G_i^o + RT \sum_i x_i \ln x_i + \sum_i \sum_{i>j} x_i x_j \sum_v \Omega_{ij}^v \ (x_i - x_j)^v \quad (4)$$

where: the first term is the reference term (${}^{ref}G_{\varphi}$), which represents, practically, the weighted average by the atomic fraction of the G of the pure substances for each element; the second term (${}^{id}G_{\alpha}$) is the energy of mixing considering only the G term of an ideal mixing, for which the enthalpy variable is equal to zero. Therefore, G can be expressed only as a function of the configurational entropy of mixing. Thus, it is not necessary to access data in the bases referring to this term, and it will be calculated only as a function of composition, not being specific to any element. These two first terms are sufficient to describe an ideal solution.

The excess contribution is given by the third term (${}^{ex}G_{\alpha}$), and all the non-ideal contributions to the G equation is described based on it. It may contain additional magnetic (${}^{mag}G_{\alpha}$) and electrical (${}^{ele}G_{\alpha}$) terms depending on the atomic interaction. The excess term can be described using Redlich-Kister polynomials [25], which are polynomial expansions to determine Gibbs free energy, where the coefficients (Ω) are experimentally estimated. The great challenge in developing the CALPHAD method lies in determining these experimental parameters (Ω) and experimental efforts generally focus on their determination and evaluation. This involves determining all relevant empirical parameters for all phases in a given combination of elements. This collection of parameters composes a CALPHAD database. The most significant limitation of CALPHAD use is the absence of available databases for some systems of interest for hydrogen storage. For example, databases containing thermodynamic data of alkaline or alkaline earth metals combined

with transition metals is still lacking. Therefore, the study of phase formation and stability of HEA containing alkaline or alkaline earth metals combined with transition metal elements is a strong motivation for HEA research.

3.1.2 Empirical methods for HEA design

HEA design methods based on the calculation and correlation of semi-empirical parameters based on the Hume-Rothery rules, in which atomic size mismatch (δ), electronegativity, and valence electron concentration (VEC) has also been used [8,11,26–28]. Yang and Zhang proposed a thermodynamic parameter (Ω) to predict the solid-solution formation ability (Equation 5). This parameter can be used to visualize the dominant term in the Gibbs free energy [8]. If $\Omega < 1$, the enthalpy of mixing dominates the Gibbs Free Energy and tends to stabilize intermetallics compounds and ordered phases. When $\Omega > 1$ the Gibbs Free Energy is more influenced by the entropic term and the formation of single solid solution is more likely.

$$\Omega = \frac{T_m \cdot \Delta S_{mix}}{\Delta H_{mix}} \qquad (5)$$

In equation 5, T_m is the melting point calculated from the average composition and ΔS_{mix} is the configurational entropy of mixing [22]. The alloy's enthalpy of mixing ΔH_{mix} can be calculated according to Miedema's extended regular solution model [29] given by equation 6:

$$\Delta H_{mix} = \sum_{i \neq j} 4 \Delta H_{ij} c_i c_j \qquad (6)$$

where, ΔH_{ij} is the mixing enthalpy of the i^{th} and j^{th} elements and C_i and C_j are respectively, the compositions of the i^{th} and j^{th}components. The enthalpy values of atomic pairs used in this work are presented in Appendix I.

By analyzing several alloys, Yang and Zhang showed a tendency towards the stabilization of single-phase solid solutions when $\Omega > 1.1$ and $\delta < 6.6\%$ [8]. The atomic size mismatch can be determined from equation 7 [10].

$$\delta = \sqrt{\sum c_i \left(1 - \frac{r_i}{\bar{r}}\right)^2} \text{x}100\% \qquad (7)$$

where i, $c_i c_i$, r_i and $\bar{r}$ are, respectively, the elements in the alloy, the atomic fraction of the i^{th} element, the atomic radii of the i^{th} element, and the weighted average atomic radius. The atomic size and melting point of the chemical elements are given in Appendix II.

To effectively correlate the atomic size difference in HEAs, given it a thermodynamic basis, Ye et al. proposed a thermodynamic rule to the design single phase HEAs [11]. Again, the central idea to Ye's rule is to evaluate the entropic dominance in controlling phase stability by using thermodynamic parameters. However, their model goes beyond the configurational entropy of mixing (S_c) and also considers the excess entropy of mixing (S_e) caused by the atomic size difference between the alloying constituents to estimate the magnitude of the total entropy of mixing (ΔS_{mix}), which is described as $\Delta S_{mix} = S_{conf} + S_{exc}$. To estimate the magnitude of the excess entropy of mixing they used the expression proposed by Mansoori et al. [30]. Mansoori's studies are based on the Hard-Spheres-Mixture model to provide equations of state for a mixture of atoms as a function of atomic packing and atom size misfit. The equations for S_e calculation are seen in Appendix III. According to the classic thermodynamics: $\Delta G = \Delta H_{mix} - T\Delta S_{mix}$ (Equation 2). If the entropic term dominates the Gibbs Free Energy function, then $\Delta G \sim -T\Delta S_{mix}$, and consequently: $|\Delta H_{mix}| / |T\Delta S_{mix}| \ll 1$. Substituting ΔS_{mix} into this inequality and rearranging the terms, the entropic dominance can be visualized through equation 8.

$$\frac{|S_e|}{S_c} \ll 1 - \frac{|H_{mix}|}{TS_c} \qquad (8)$$

The inequality tends to be satisfied if the temperature and S_c on the right side of equation 8 are increased. Despite that, generally, this short analysis is insufficient because other terms play an essential role in the phase stability. Therefore, in a second report, Ye et al. proposed a single thermodynamic rule to the design single-phase HEAs [12]. The authors proposed a dimensionless parameter (φ) that is expressed by equation 9.

$$\varphi = \frac{S_c - \frac{\Delta Hmix}{Tm}}{|S_e|} \quad (9)$$

where ΔH_{mix} is the enthalpy of mixing estimated by the Miedema's model (Equation 6); S_c is the configurational entropy of mixing (Equation 1); S_e is the excess entropy of mixing calculated using Mansoori's model and T_m is the alloy's mean melting temperature weighted by its atomic fraction c_i. By comparing experimental data from the literature, they found that a single-phase solid solution is found when the φ parameter is maximized as can be seen in Figure 3.1. A critical value of $\varphi_{crit} = 20$ was found. Above this critical value, the formation of a single-phase solid solution is very likely. For φ values distributed in a range between 11 and 20, single-phase and multiphase alloys were found. Finally, when $\varphi < 10$ the enthalpy of formation is more relevant than the entropic term, and intermetallic compounds are likely to be formed.

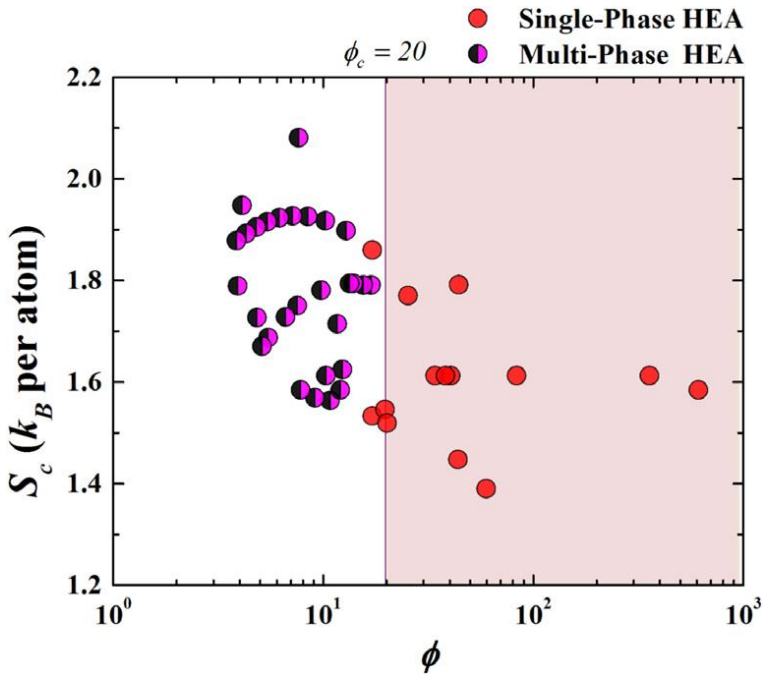

Figure 3.1 – The plot of S_c versus φ for a variety of HEAs with either a single- or multi-phased structure. From reference [12].

The crystal structure of single-phase HEAs can be successfully predicted using the valence electron concentration (VEC) defined by Equation 10.

$$\mathrm{VEC} = \sum_i c_i \cdot (\mathrm{VEC})_i \quad (10)$$

where $(\mathrm{VEC})_i$ and c_i is the valence electron concentration and the atomic fraction of element, respectively. According to Guo et al. [9], alloys with $\mathrm{VEC} < 6.87$ tend to form body-centered cubic solid solutions, whereas face-centered cubic (FCC) solid solutions are expected for $\mathrm{VEC} > 8$.

3.2 HEA-based metal hydrides

3.2.1 Fundamental thermodynamic aspects of metal hydrides

This section is a brief overview of the thermodynamics aspects of the hydride formation obtained directly from a reaction between the gaseous H_2 and a host metal. Equation 11 describes the reversible reaction of the hydrogen loading and unloading where a hydride-forming metal (M) interacts with hydrogen and form a metal hydride (MH_x). Note that Q is the heat of reaction. Usually, the hydrogen absorption reaction is exothermic, while desorption is an endothermic process.

$$M + \frac{x}{2}H_2 \Leftrightarrow MH_x + Q \quad (11)$$

The steps which involve the metal hydride formation starts with surface events. At first, there is physical adsorption of the H_2 molecule on the material's surface through Van der Waals interactions, followed by a chemical dissociation of the hydrogen molecule. Then the hydrogen enters the metal lattice and forms a solid solution phase. This solid solution is called α phase, where the hydrogen is randomly distributed in the metal lattice. At lower concentrations, the formation of the solid solution has an ideal solution behavior, and the thermodynamic equilibrium is given by the equality of the chemical potential of the molecular hydrogen (μ_{H_2}) and the chemical potential of the atomic hydrogen in solution (μ_H). The equilibrium is represented by equation 12:

$$\frac{1}{2}\mu_{H_2}(p, T) = \mu_H(p, T, C_H) \quad (12)$$

where p and T are intensive properties of the system and C_H is the hydrogen concentration given in H/M.

For infinite dilution, assuming an ideal gas and a system where the H_2 molecules are dissociated into atoms before becoming dissolved in metals, the equilibrium can be represented by Sievert's law (equation 13):

$$p_{H_2}^{1/2} = K_s \qquad (13)$$

where K_s is a constant written in function of the entropy and enthalpy of solution. The entropy term is roughly constant for all metal-hydrogen systems since its effects are associated primarily with the slight entropy loss of gaseous hydrogen. Therefore, the heat of solution has a central role in hydrogen absorption. This is very important since the enthalpy of solution is closely associated with the coarse electronic structure of the host metal [4]. It is essential to mention that Sievert's law is only valid if the number of interstitial sites per metal atoms is much bigger than the number of sites occupied by hydrogen atoms.

At higher hydrogen concentrations, the effects of interactions between hydrogen atoms in the crystal lattice become important, and then a higher hydrogen concentration phase nucleates, the β phase. The pressure which α and β coexist is called plateau or equilibrium pressure (P_{eq}) and is given by the van't Hoff equation (equation 14).

$$\ln P_{eq} = \frac{\Delta H}{RT} - \frac{\Delta S}{R} \qquad (14)$$

In equation 14, the entropy of the $\alpha \rightarrow \beta$ transition (ΔS) is usually not strongly affected by the nature of the host metal and is considered constant. However, the enthalpy of the $\alpha \rightarrow \beta$ transition has a strong influence of the host metal and H-H interactions, where enthalpy values are dependent of elastic and electronic contributions and vary with hydrogen concentration. The thermodynamic aspects of metal hydride systems can be experimentally estimated by acquiring pressure-composition isotherms curves (PCI). The schematic isothermal curve is shown on the left side of figure 3.2., where $T_1 < T_2 < T_3$. By plotting the equilibrium pressure logarithm against the reciprocal temperature $(1/T)$ for some isothermal curves (the right side of figure 3.2), the plateau

enthalpies are obtained from the plot's slope. This plot is called van't Hoff plot and is a graphical visualization of equation 14.

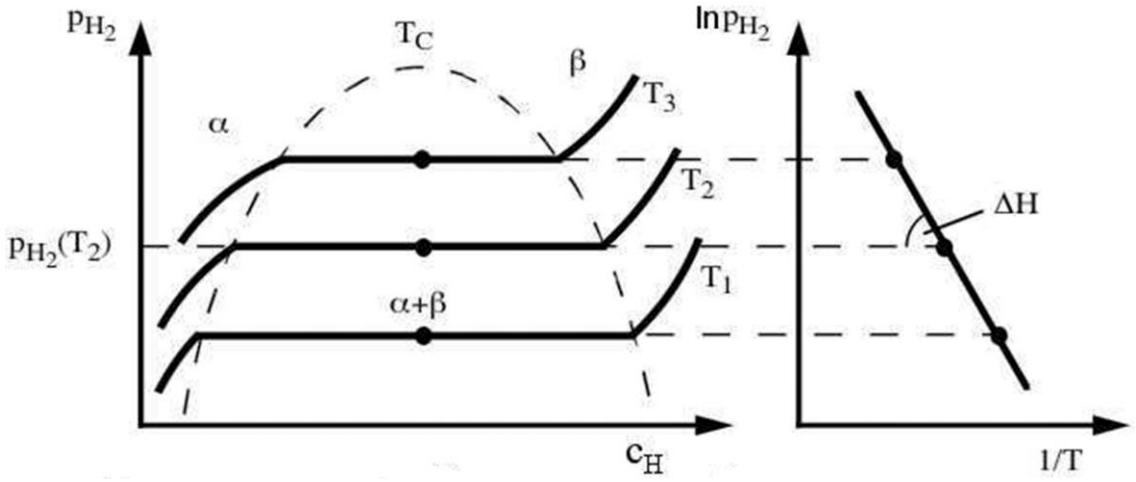

Figure 3.2 – Schematic PCI curve (left side) and a van't Hoff plot (right side). Adapted from [31].

3.2.2 High entropy metal hydrides – A brief overview

In the last decade, several HEAs with outstanding mechanical and functional properties have been reported in the literature [32,33]. Among the functional properties reported, HEA-based metal hydrides for solid-state hydrogen storage are attracting attention. The vast compositional field opened by HEAs' advent may lead to new alloys with optimized hydrogen storage properties. Thus, numerous investigations are being conducted to improve and control the metal hydride properties such as hydrogen storage capacity, hydrogenation/dehydrogenation kinetics, cyclic stability, and operating temperature and pressure.

One important group of HEAs based metal hydrides belongs to the intermetallic compounds, being the Laves phase-type intermetallics the most common. These intermetallics have AB_2 stoichiometry, where A and B are the larger and smaller atoms, respectively, and three distinct polytypes are often observed: the cubic $MgCu_2$ type (C15), the hexagonal $MgZn_2$ type (C14), and the hexagonal $MgNi_2$ type (C36) [34]. Often studied

for hydrogen applications, is not uncommon the use of the representative compositions AB_5, AB_2, AB, and A_2B, where the A elements have high affinity with hydrogen (i.e., are known to form stable hydrides such as Ti, V, Nb, Zr) while B has a lower affinity with hydrogen such as Fe, Cr, Mn, Ni, Co etc.

One of the earliest investigations of HEA-based metal hydrides reports the synthesis of several alloys of the $CoFeMnTi_xV_yZr_z$ system by arc-melting, which crystallized as C14-type Laves phase ($MgZn_2$ type, $P6_3/mmc$ space group) [35]. The alloys absorbed hydrogen at room temperature and the maximum capacity was about 1.7 wt.% achieved by the $CoFeMnTiVZr_{2.3}$ alloy. According to the authors, the hydrogen capacity is strongly dependent of the affinity between the alloy elements and hydrogen. In another work, Kunce et al. synthesized the ZrTiVCrFe HEA by Laser Engineered Net Shaping (LENS), followed by an annealing heat treatment at 1000°C for 24h [36]. They found a dual-phase structure with a major C14-type Laves phase and a minor amount of α-Ti. The maximum measured hydrogen storage capacity was 1.56 wt.%.

By induction melting, Young et al. successfully synthesized the $Zr_{21.5}Ti_{12}V_{10}Cr_{7.5}Mn_{8.1}Co_8.1Ni_{32.2}Sn_{0.3}Al_{0.4}$ with a major C14-type Laves phase and the $Zr_{25}Ti_{6.5}V_{3.9}Mn_{22.2}Fe_{3.8}Ni_{38}La_{0.3}$ alloy with a single C15-type Laves phase ($MgCu_2$ type, space group Fd-3m) [37]. The acquisition of PCI Isotherms at 30 °C showed a reversible capacity of 1.32 wt.% for the first alloys and 1.44 wt.% for the second one. Room temperature operating conditions were applied by Edalati et al. working with the TiZrCrFeMnNi HEA [13]. By arc-melting, they synthesized the equiatomic alloy, which crystalized as a major C14-type Laves phase with minor Ti and Ni-rich precipitates. PCI measurements at room temperature showed a reversible hydrogen capacity of the 1.7 wt.%, which represents a hydrogen-to-metal ratio equals 1 with almost no hysteresis.

The hydrogen storage properties of different single BCC phase HEAs has also been reported. Zlotea et al. synthesized by arc melting the TiZrNbHfTa alloy and obtained a single BCC structure [16]. In situ synchrotron X-ray diffraction under hydrogen pressure showed two-stage hydrogen absorption reaction. Firstly, a body-centered tetragonal (BCT) monohydride was formed. Subsequently, face-centered cubic (FCC) hydride with H/M = 2 (CaF_2-type structure) was formed. The alloy's hydrogen capacity was about 1.65 wt.%.

Sahlberg et al. reported outstanding hydrogen uptake for the TiVZrNbHf HEA produced by arc-melting [19]. This alloy also crystallized as a single BCC solid solution and hydrogenation measurements showed a hydrogen storage capacity of 2.7 wt.% (H/M = 2.5) at 299°C and 5.3 MPa of H_2. The hydride formed presented a BCT structure, which is a distorted form of the FCC (CaF_2-type structure) hydride [18]. The authors argued that the high storage capacity could be related to high local lattice strain caused by the large atomic size mismatch (δ ~ 6.8%), which would favour the allocation of hydrogen in the tetrahedral and octahedral interstitial sites. Nygård et al. published a study that correlate the local lattice strain with hydrogen capacity [38]. Several single BCC alloys of composition $TiVZr_zNbTa_{1-z}$ and $TiVZr_{1+z}Nb$ were synthesized by arc-melting. The atomic size mismatch varied between 3.5% and 6.34% for the studied alloys. After hydrogenation, all alloys form a dihydride with a CaF_2-type face-centered cubic structure with hydrogen uptake close and never exceeding the hydrogen-to-metal ratio 2. This indicates no correlation between alloy hydrogen uptake and local lattice strain.

A recent discussion about the formation and stability of the HEAs based hydrides was also proposed by Nygård et al. [39]. By analyzing trends of some single BCC HEAs that are chemically related to the ternary system TiVNb system, they proposed that the hydrogen storage properties are linked to the valence electron concentration (VEC) of the alloy. Figure 3.4 displayed the manometric and volumetric hydrogen uptake (H / M) for each alloy ploted against the VEC values. For VEC values lower than 5.00, the hydrogen uptake is close 2 and the BCC alloy can assume the FCC dihydride structure. On the other hand, for VEC values greater than 5 the hydrogen content is lower and theses alloys do not assume the FCC dihydride structure.

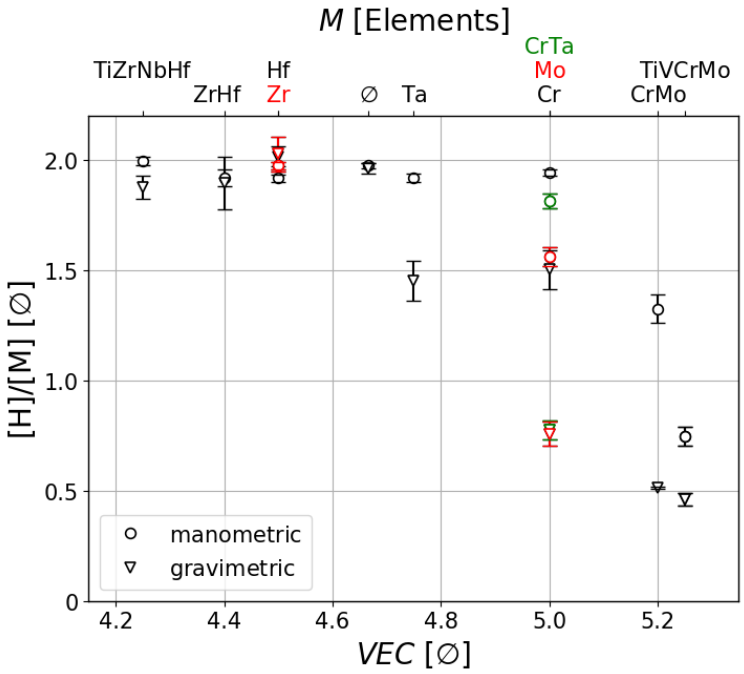

Figure 3.3 – Hydrogen uptake and valence electron concentration plotted for each alloy: $TiVCrMoH_x$, $TiZrNbHfH_x$, $TiVNbMH_x$, M ∈ {Ø; Cr; Zr; Mo; Hf;Ta}, $TiVZrNbHfH_x$ (M = ZrHf), $TiVCrNbMoH_x$ (M = CrMo) and $TiVCrNbTaH_x$. Adapted from [39].

3.3 Mg-containing high entropy alloys for hydrogen storage

The development of HEA containing alkaline or alkaline earth metals combined with transition metal elements is a challenge for the community committed in the study of multicomponent alloys. For example, Sun et al. analyzed the effect of light elements, such as Al, Ti, Si, Li, and Mg, in several low-density HEAs produced by conventional casting, rapid solidification process (laser cladding) and mechanical alloying [40]. They concluded that the addition of magnesium usually leads to the formation of intermetallic phases during solidification. However, these intermetallics may be dissolved into a solid solution by applying a secondary non-equilibrium process such as high energy ball milling.

HEBM can also suppress the formation of secondary phases allowing the formation of single-phase alloys that would not be possible to be obtained by conventional casting [41–43]. Besides that, melting Mg-containing HEAs is challenging because of the

low boiling temperature of Mg (1091 °C) when compared to the transition metals, especially the refractory elements. For instance, Youssef et al. produced a low-density $Al_{20}Li_{20}Mg_{10}Sc_{20}Ti_{30}$ (2.67 g/cm^3) HEA by HEBM from pure elemental powders [44]. After HEBM process (2 hours under cryogenic temperature and 14 hours at room temperature), a single-phase FCC structure was formed. The authors also showed that the FCC phase transforms into a hexagonal close-packed (HCP) structure after annealing at 500°C for 1 hour.

Undoubtedly, the addition of light metal elements such as magnesium and aluminum in HEA metal hydrides may be beneficial to increase their gravimetric capacities by decreasing the alloys' densities. To the best of our knowledge, Zepon et al. were the first to report the synthesis of Mg-containing BCC HEAs for hydrogen storage by HEBM [45]. They reported the study of $MgZrTiFe_{0.5}Co_{0.5}Ni_{0.5}$ alloy which was synthesized by HEBM under argon atmosphere (0.7 MPa) and hydrogen pressure (3.0 MPa). The alloys synthesized under argon presented a BCC single-phase structure and when subjected to hydrogenation (350 °C and 2.0 MPa of H_2) absorbed 1.2 wt.% hydrogen in approximately one hour. The hydrogenation was accompanied by an incomplete transformation from BCC solid solution to FCC hydride. However, the FCC hydride was directly obtained by using high-energy ball milling under hydrogen pressure.

In another work, Marques et al. [46] reported the synthesis of Mg-containing MPEAs by high energy ball milling under argon atmosphere (0.7 MPa) and under high hydrogen pressure (3.0 MPa). $MgTiNbCr_{0.5}Mn_{0.5}Ni_{0.5}$ and its derivative quaternary $Mg_{0.68}TiNbNi_{0.55}$ alloy were synthesized. Both alloys formed a mixture of phases with major BCC structure when milled under argon, while the FCC hydride alongside with $MgNiH_4$ were observed after synthesis under hydrogen pressure. Although having mixture of phases, in the $Mg_{0.68}TiNbNi_{0.55}$ alloy, the contribution of the FCC hydride in the gravimetric capacity is greater than that for the $MgTiNbCr_{0.5}Mn_{0.5}Ni_{0.5}$ alloy.

4 MATERIALS AND METHODS

This work was divided into three steps with well-defined goals. In each step, appropriate the design method, synthesis method, and characterization techniques were chosen. Consequently, in this thesis the methodology was divide into three steps which address a chapter with the same name in the results and discussion (Session 5). Firstly, the HEBM was employed to produce a set of alloys of the Mg-V-Al-Cr-Ni system. This approach allows to investigate the phase stability of different alloys within a same system and evaluate their hydrogen properties. In a second moment, a semi-empirical approach was employed to design a single-phase BCC alloy from the Mg-Al-Ti-Mn-Nb system with high hydrogen affinity. Finally, CALPHAD method was employed to design alloys based on the $(TiVNb)_{100-x}M_x$ system (where M = Cr, Mn, Fe, Ni and Co) with tunable H storage properties. The detailed description of the methodology used for each part is presented in the following sections.

4.1 Design of HEAs from the Mg-V-Al-Cr-Ni system

4.1.1 System selection

The periodic system of elements can be classified into two groups of interest: hydride and non-hydride-forming elements. Where the criteria to set the hydride or non hydride-forming was the formation enthalpy of binary metal hydrides (ΔH_f^o) [31]. The figure 4.1 illustrates an arrangement in the periodic system of elements, where the elements in red are considered hydride-forming and their enthalpy of formation is very negative, the elements in white had small positive or negative enthalpy values, while the the blue elements have positive heating values and do not form binary metal hydrides.

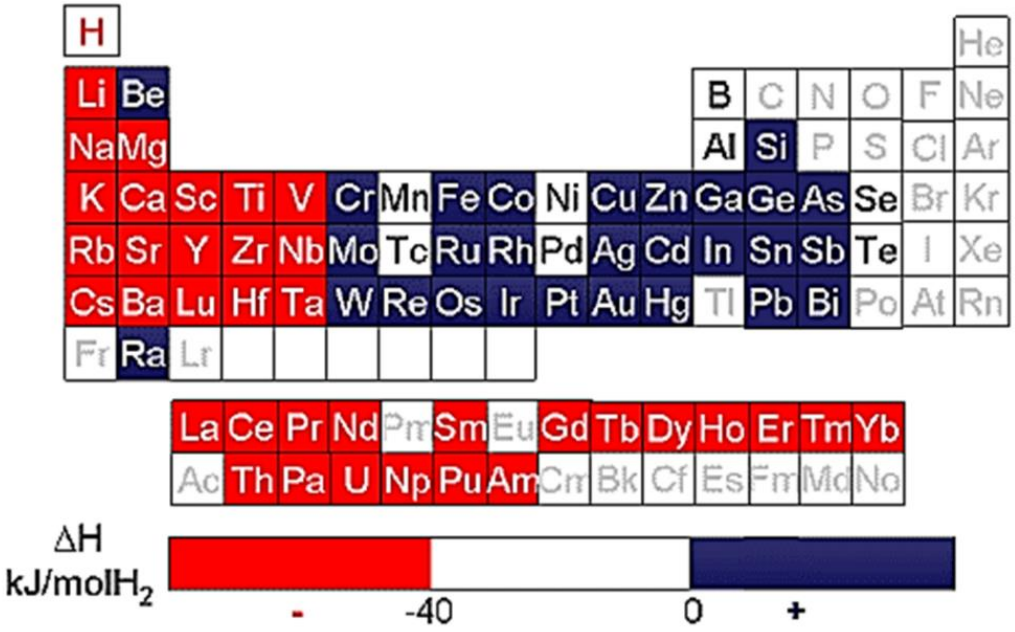

Figure 4.1 – Periodic table indicating the hydride-forming elements (red), elements with a moderate enthalpy of hydride formation values (white), and non-hydride-forming elements (blue). Adapted from reference [31].

The goal here is to produce lightweight BCC-HEAs for hydrogen storage applications with high hydrogen gravimetric capacity. To reduce the alloy's molecular weight, the addition of light metal elements such as magnesium and aluminum may be beneficial. Therefore, combining the Mg and Al lightweight elements with transitions metals was set as a criterion to obtain lightweight alloys.

It is important to mention that Mg and Al are, respectively, hydrides and non-hydride forming elements. The other alloying elements' choice was based mainly on their ability or not to form a binary metal hydride. The basic idea was to balance Mg and Al with alloying elements with hydride-forming elements and non-hydride forming elements. In this study, vanadium, which is a BCC metal, was selected as the hydride forming element. Chromium and Nickel were selected as non-hydride-forming elements. Cr is a BCC metal with a positive enthalpy of hydride formation, while Ni is a FCC metal and it was selected due to its ability to form a complex hydride with Mg, which could favor the mixture of Mg and Ni with H in the final alloy [47]. Therefore, the unprecedented Mg-V-Al-Cr-Ni system was selected to be investigated.

To evaluate the possible phases that could be formed, ternary, quaternary, and quinary equiatomic alloys of the Mg-V-Al-Cr-Ni system were produced by HEBM under hydrogen pressure. Only alloys containing Mg and V (hydride formers) were synthesized. The equiatomic MgVAlCrNi alloy was prepared by HEBM under H_2 pressure and argon atmosphere, and its hydrogen storage properties were evaluated. Additionally, non-equiatomic alloys of the Mg-V-Al-Cr-Ni were also synthesized to evaluate the effect of stoichiometry variation on the phases formed and hydrogen storage properties. The following alloys were studied in this work: MgVAl, MgVCr, MgVNi, MgVAlCr, MgVAlCr, MgVAlNi, MgVCrNi, MgVAlCrNi, $Mg_{28}V_{28}Al_{19}Cr_{19}Ni_6$ and $Mg_{26}V_{31}Al_{31}Cr_6Ni_6$.

4.1.2 Alloy synthesis

HEBM was adopted as the process route by taking into account three main aspects: (i) HEBM is a solid state process route which consists of repeated phenomenon of cold welding and fracturing between powder particles [48]. Since melting Mg-containing HEAs is challenging because of the low boiling temperature of Mg (1091 °C) when compared to the refractory transition metals, HEBM can be considered a suitable process route; (ii) HEBM can be useful for producing HEAs containing light elements, such as Al, Ti, Si, Li, and Mg combined with transitions metals because it can suppress the formation of secondary phases; (iii) the mechanochemical alloy synthesis by HEBM can be conducted under an inert atmosphere, for instance, under argon atmosphere. Moreover, the HEBM can be applied to directly prepare metal hydrides by a solid–gas reaction by mechanical milling in a reactive H_2 atmosphere. This processing route is named reactive high-energy ball milling (RM) [49].

The HEBM process was carried out in a Fritsch P6 planetary mill with a stainless-steel sealed vial (internal volume of 250 cm^3) and 25 stainless steel balls (15 with 8 mm diameter and 10 with 10 mm diameter). The ball-to-powder weight ratio, rotating speed, and milling time were 20:1, 600 rpm, and 24 hours, respectively. Pure elements purchased from Alfa Aesar were used as starting material: magnesium powder, -20+100 mesh (99.8%), vanadium powder -325mesh (99.5%), aluminum granules, -1 mm (99.7%), chromium powder, -325 mesh (99.5%) and nickel powder, -325 mesh (99.5%). All the

samples were handled inside a MBRAUN glovebox under a protective argon atmosphere with H_2O and O_2 levels below 0.1 ppm. The reactive HEBM was carried out under 30 bar of H_2 (99.999%) pressure, while 7.0 bar of argon (purity > 99.995%) atmosphere was used for inert mechanical milling.

4.1.3 Structural and Thermal Characterization

Structural characterization of the HEBM samples was performed by X-ray Diffraction (XRD) using a Bruker D8 Advance ECO diffractometer equipped with a Cu tube. Scanning Electron Microscopy (SEM) was performed in a FEI Inspect S50 operating at 25 kV, equipped with Energy Dispersive Spectroscopy (EDS) from EDAX. Transmission electron microscopy (TEM) using a field emission gun (FEI-Tecnai G2F20) microscope was used for structural observation in the nanoscale. The hydrogen desorption was evaluated by differential scanning calorimetry (DSC) coupled with quadrupole mass spectrometry (QMS) and thermogravimetric analysis measurements (TGA) in a Netzsch Simultaneous Thermal Analyzer (STA) 449 operating at a constant heating rate of 10 K/min under purified argon flow (25 ml/min).

4.2 Design of single BCC HEA from the Mg-Al-Ti-Mn-Nb system

4.2.1 System selection and Design Method

Based on previous results of the Mg-Al-V-Cr-Ni system, which showed poor hydrogen affinity, a new HEA system was proposed for this part of the work, namely Mg-Al-Ti-Mn-Nb. In this new system, Mg and Al were kept because of their light weight. Two strong hydride-forming elements (Ti and Nb) and only one non-hydride forming element (Mn) were added.

An alloy composition of the Mg-Al-Ti-Mn-Nb system was designed by calculating the semi-empirical parameters (φ, VEC, mean enthalpy of hydride formation and mean enthalpy of H solution) of 1326 alloys with $(TiNb)_x(AlMn)_yMg_{1-x-y}$ stoichiometry. The aim

of the alloy design was to select a composition with high tendency to form single BCC structure and high hydrogen affinity.

4.2.2 Alloy synthesis

The designed and equiatomic alloys were synthesized by HEBM. High-purity Mg (99.8%), Al (99.7%), Ti (99.5%), Mn (99+%), Nb (99.8%) powders were ball milled under 7.0 bar of argon (purity>99.995%) or a 30.0 bar of hydrogen ((99.999%). It was used a Fritsch – P6 planetary ball mill, with a ball-to-powder weight ratio of 20:1, rotating speed of 600 rpm, and milling time of 24h. All the manipulations were carried out in a glove box under argon atmosphere with O_2 and humidity contents about 0.1 ppm.

4.2.3 Structural characterization

Phase identification was performed by XRD analysis using a D8 Advanced Eco diffractometer with KαCu radiation, operating at 40 kV and 20 mA. The particles' chemical composition and homogeneity were evaluated by scanning electron microscopy (SEM) using a FEG Philips XL-30 microscope equipped with Bruker Nano X-Flash 6|60 EDS detector and by transmission electron microscopy using a FEG-FEI Tecnai G^2F20 microscope equipped with EDAX-EDS detector. The TEM sample was prepared by dispersion of the powders onto a carbon-coated copper grid.

4.2.4 Hydrogen storage properties measurements

The hydrogen storage properties of the designed alloy ($Mg_{12}Al_{11}Ti_{33}Mn_{11}Nb_{33}$) were evaluated through volumetric techniques using a Sievert-type apparatus SETARAM® PCT-Pro model. Before hydrogenation, an activation process was performed. The activation procedure consisted of keeping the sample under a dynamic vacuum at 450°C for 3 hours. Desorption measurements were carried out using a Netzsch Simultaneous Thermal Analyzer STA-449C Jupiter Unit equipment that combines differential scanning calorimetry (DSC), thermogravimetric analyses (TGA), and a

quadrupole mass spectrometer (QMS) for H_2 detection. The thermal analysis was carried out using a heating rate of 10ºC min^{-1} and an argon flow of 50 $mL.min^{-1}$.

4.3 Design of BCC HEA for hydrogen storage by CALPHAD: Addition of non-hydride forming element to the Ti-V-Nb system

4.3.1 System selection and design method

This work aims to evaluate the effects of introducing a non-hydride forming metal to a BCC system composed of hydride forming elements (Ti-V-Nb). The addition of different non-hydride forming elements, namely Cr, Mn, Fe, Co and Ni, into the Ti-V-Nb system was investigated through CALPHAD method. The Thermo-Calc software with the TCHEA3 database was employed. Thermodynamic calculations were conducted to investigate which element among the non-hydride forming elements could be added in different fractions into the Ti-V-Nb system without leading to the formation of second phases. As will be exposed in section 5.3, Cr was the selected element and three alloys with different fractions of this element were produced and investigated.

4.3.2 Alloy synthesis

The refractory HEA family consists of alloys containing the following elements: Cr, Hf, Mo, Nb, Ta, Ti, V, W, and Zr. These elements have high melting points and are often applied to develop new high-temperature structural metals [32]. For refractory alloys, the use of the arc-melting technique can be considered a suitable process route. Thus, the $(TiVNb)_{100-x}Cr_x$ alloys were synthesized by arc melting under an inert argon atmosphere, starting from pure elements purchased from Alfa-Aesar: Ti (99.95%), V (99.7%), Cr (99%), and Nb (99.8%). To ensure the composition homogeneity, the samples were turned over and remelted five times.

4.3.3 Structural characterization

Initial crystallographic information was obtained by X-ray diffraction (XRD) using a Bragg-Brentano diffractometer (Bruker D8 Focus) with Cu-Ka radiation. Prior the XRD analysis the ingots were crushed inside a glovebox under argon atmosphere using a stainless-steel mortar and pestle. The microstructure was evaluated by scanning electron microscopy (SEM) using a FEI-Inspect S50 electron microscope equipped with an energy dispersive spectroscopy (EDS) detector attached. For the EDS measurements, a compositional average was estimated by collecting at least five representative points for each microstructure contrast. The SEM microscope was also equipped with an electron backscattered diffraction (EBSD) detector. The EBSD technique was applied to correlate the microstructure with crystallographic information. For microstructural and compositional characterization by SEM, the samples were sectioned and manually polished.

4.3.4 Hydrogen storage properties measurements

PCI absorption/desorption isotherms were performed using a Sievert-type apparatus PCT Pro-SETARAM operating at room temperature (~24 °C). The hydrogen absorption kinetics measurements were performed using a homemade Sievert-type apparatus operating at room temperature (~24 °C) and 2000 kPa of H_2. Before the hydrogen measurements, the samples are crushed using a stainless-steel mortar and pestle inside a glove-box machine with H_2O and O_2 levels below 0.1 ppm. The kinetics measurement was carried out without any activation process. Prior to the PCI measurements, a heat treatment at 450°C under dynamic vacuum for 2h was carried out.

5 RESULTS AND DISCUSSION

5.1 Design of HEAs from Mg-V-Al-Cr-Ni system

This section presents a strategy to produce lightweight HEAs for hydrogen storage based on the Mg-V-Al-Cr-Ni system. Considering the lightweight of Mg and Al, the basic idea was to apply a systematic methodology to verify the influence of different compositions of the Mg-V-Al-Cr-Ni system on the phase formation and hydrogen storage behavior. The final goal was to obtain a single-phase BCC alloy suitable for hydrogen storage applications.

5.1.1 Synthesis and characterization of ternary, quaternary, and quinary equiatomic alloys

Figure 5.1 shows the XRD patterns of the equiatomic ternary MgVAl, MgVCr, MgVNi, quaternary MgVAlCr, MgVAlNi, MgVCrNi, and quinary MgVAlCrNi alloys after HEBM under hydrogen pressure. These patterns show that the ternary MgVAl and MgVCr alloys are composed of major BCC phases with a lattice parameter of 3.091(4) Å and 2.965(9) Å, respectively. The number in parentheses is the error on the last significant digit. Both compositions showed a small fraction of magnesium hydride (MgH_2) phase. The ternary MgVNi alloy presented a XRD pattern in which only the Mg_2NiH_4 complex hydride could be indexed. A broadband in the 2θ range of 37° to 50 ° was also observed, which may indicate the formation of an amorphous phase. The XRD pattern of the quaternary MgVAlCr suggests the formation of two BCC structures. A major one with a = 3.028(2) Å and the second one in smaller fraction with a = 2.904(9) Å. The as-milled MgVAlNi has a major BCC phase (a = 2.913(5) Å) and two unidentified broad peaks at 32° and 40°. The quaternary MgVCrNi alloy presents mostly a BCC phase (a = 2.915(3) Å) and a small fraction of Mg_2NiH_4 complex hydride. Finally, the quinary MgVAlCrNi alloy exhibited a single BCC phase structure with a lattice parameter a = 2.952(3) Å.

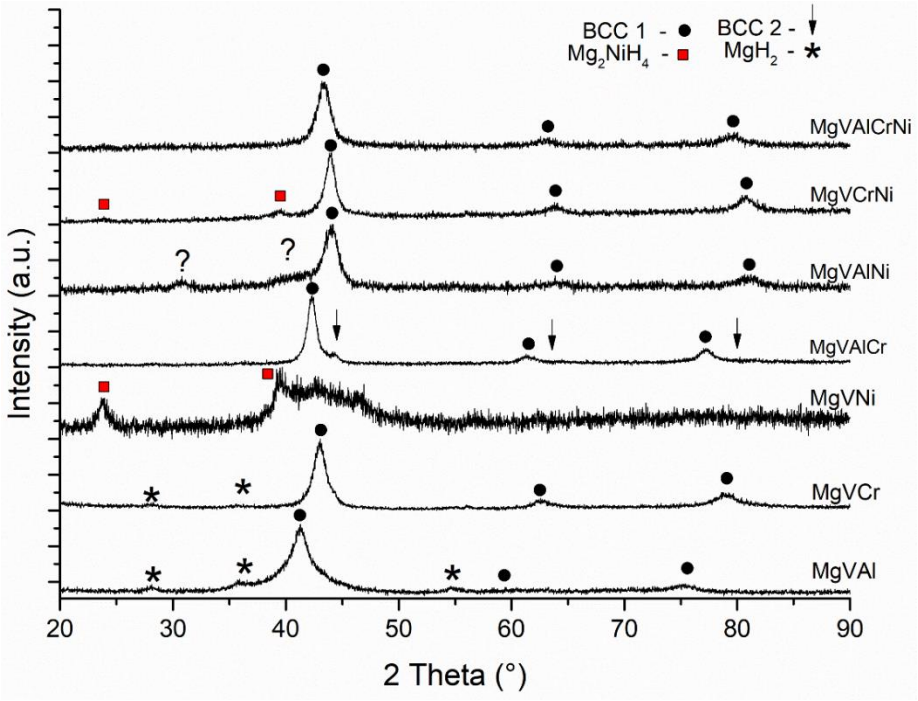

Figure 5.1 – XRD patterns for the ternary, quaternary, and quinary equiatomic compositions of the Mg-V-Al-Cr-Ni system after HEBM under hydrogen pressure.

Figure 5.2 presents the thermal analysis for the studied alloys. The ternary MgVAl (Figure 5.2(a)) alloy presented an endothermic peak related to hydrogen release at 356 ºC. The mass loss of this alloy during hydrogen desorption was about 1.35 wt.%. This was the highest hydrogen desorption capacity observed among all the alloys studied. It is worth noting that this alloy presents some fraction of MgH_2, indicating that this phase might be responsible for part of the hydrogen storage capacity. However, a shoulder in the endothermic peak can be seen for higher temperatures, suggesting that more than one phase might be responsible for the hydrogen desorption for this alloy.

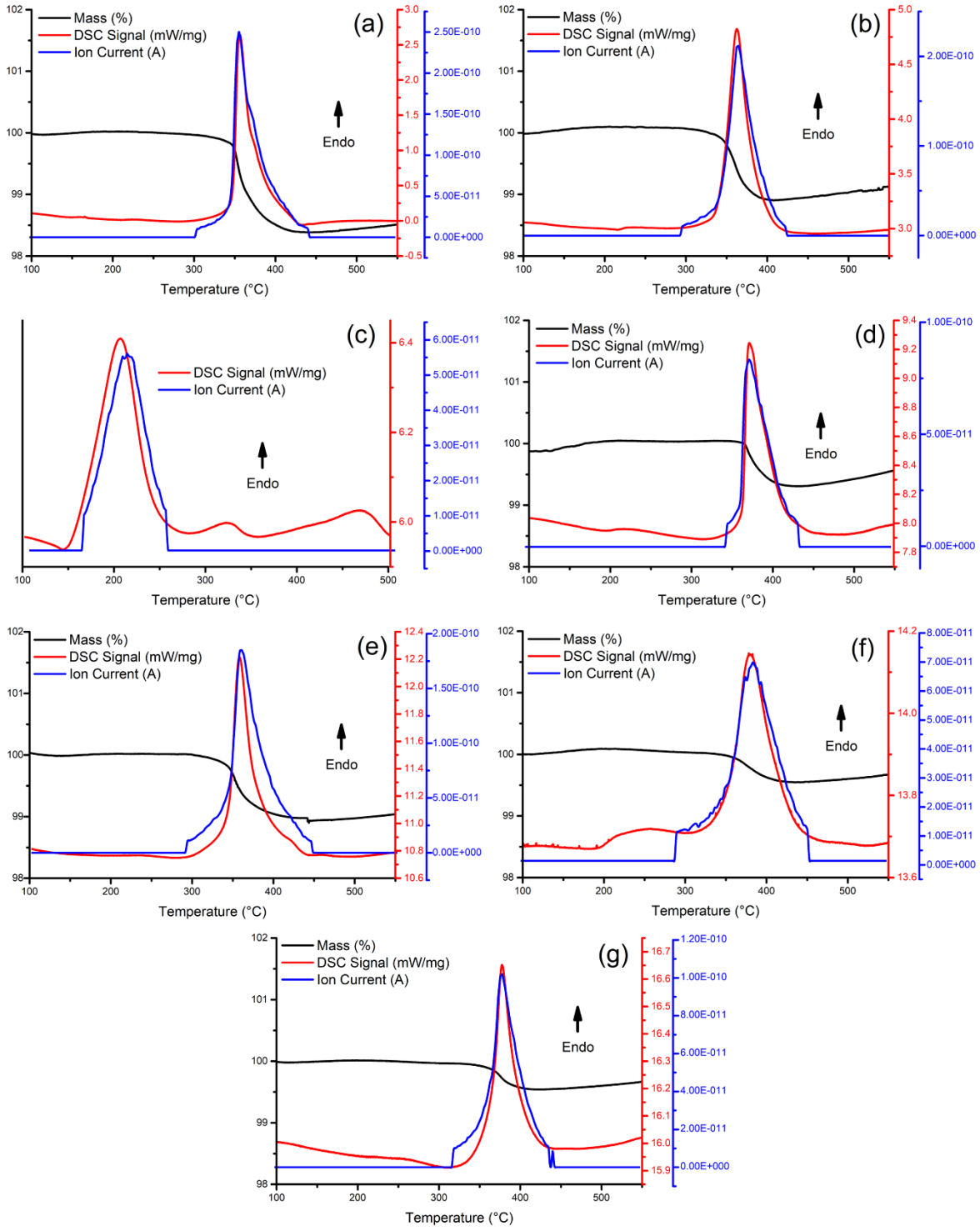

Figure 5.2 – TGA (black line), DSC (red line) and QMS (blue line) curves for (a) MgVAl, (b) MgVCr, (c) MgVNi, (d) MgVAlCr, (e) MgVAlNi, (f) MgVCrNi and (g) MgVAlCrNi alloys.

The ternary MgVCr alloy also presented an endothermic event related to hydrogen desorption at around 362 ºC (Figure 5.2(b)). The mass loss for this sample was 0.98 wt.%. The ternary MgVNi alloy presented an endothermic peak related to hydrogen desorption at around 200 ºC, a lower temperature compared to the other alloys. This endothermic peak could be related to the desorption of Mg_2NiH_4 since this is the typical desorption temperature range for this hydride [47]. The mass loss for this sample was quite small and could not be accurately measured by TGA. The MgVAlCr, MgVAlNi, and MgVCrNi quaternary alloys presented endothermic peaks related to hydrogen desorption at 372 ºC, 356 ºC, and 378ºC, with mass loss of 0.63 wt.%, 0.84 wt.%, and 0.34 wt.%, respectively. Finally, the single-phase MgVAlCrNi alloy presented an endothermic peak related to hydrogen desorption at 377 ºC. The hydrogen desorption capacity of this alloy was only 0.30 wt.%, indicating that the BCC phase formed has a low hydrogen storage capacity.

In the ternary and quaternary systems, the formation of second phases was associated with MgH_2 and Mg_2NiH_4 (Figure 5.1). The binary phase diagrams show that V, Ni, and Cr have almost no solubility in Mg as consequence of the enthalpy of mixing between these elements (Table 5.1). The enthalpy of mixing between Mg-V (+23 kJ/mol) and Mg-Cr (+24 kJ/mol) are very positive, which result in almost incomplete solubility of Cr and V in Mg. The slightly negative enthalpy of mixing between Mg and Ni (-4 kJ/mol), makes the Mg-Ni binary diagram to be composed of different binary intermetallics, with Mg_2Ni being the Mg-rich intermetallic of this system. Al is the only element that forms solid solution (~10 at.% at 700 ºC) with Mg. Since the enthalpy of mixing of all the Al-V-Cr-Ni pairs are considerably more negative, the formation of Mg-rich second phase is more likely due to the low affinity between Mg, Cr and V. Interestingly, only a single BCC solid solution was formed for the quinary MgVAlCrNi HEA. The entropy effect might be the reason for supressing the formation of Mg-rich hydrides. Therefore, the next section will present the structure characterization and thermal stability of this novel single phase MgVAlCrNi HEA.

Table 5.1 – Binary enthalpy of mixing (kJ/mol) calculated by Miedema's model [29].

	V	Al	Cr	Ni
Mg	23	-2	24	-4
V		-10	-2	-18
Al			-10	-22
Cr				-7

5.1.2 Structural characterization and hydrogen storage behavior of the MgVAlCrNi HEA

Figure 5.3a shows the secondary electrons SEM image, and Figure 5.3b the corresponding EDS spectrum of the MgVAlCrNi alloy synthesized by HEBM under hydrogen pressure. The powder has heterogeneous particle size ranging from 0.5 to 15 μm. Table 5.2 shows the chemical composition of the alloys measured by SEM-EDS in different regions with low magnification. The measured chemical composition of the synthesized alloy is close to the nominal composition.

By using the average chemical composition of the alloy measured by SEM-EDS, the Ω = 3.63, δ = 9.7 %, and VEC = 5.3 parameters were calculated. The calculated VEC value is within the range where the BCC phase is stabilized (VEC ≤ 6.87), as proposed by Guo et al. [9], which is in agreement with the XRD pattern found for this alloy (Figure 5.1). Yang and Zhang proposed that single-phase alloys are expected to be formed when δ < 6.6% and Ω > 1.1 [8]. One can see that the Ω value is higher than the condition proposed by the authors. However, the atomic size mismatch (δ) is out of the range in which single-phase alloys are expected.

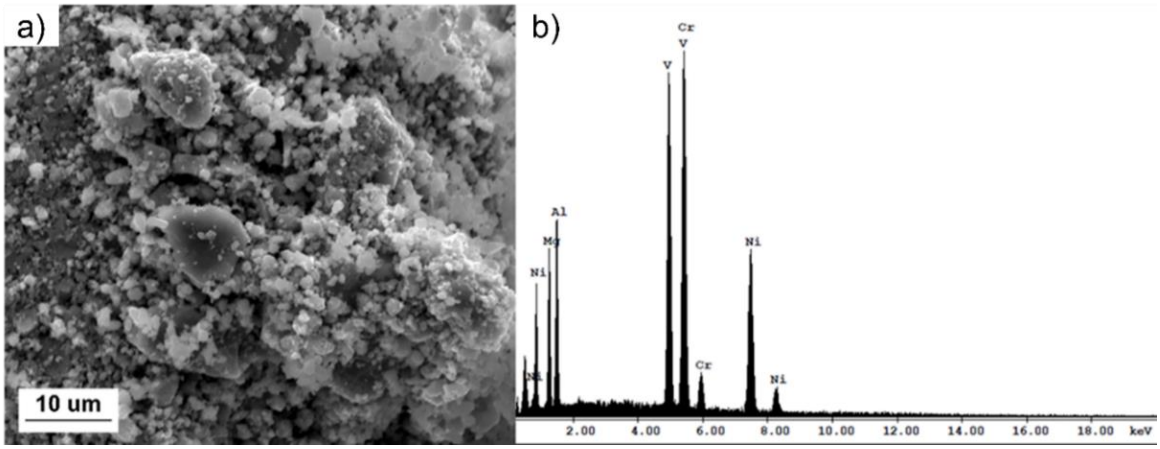

Figure 5.3 – SE-SEM image of the MgVAlCrNi alloy produced by HEBM under hydrogen pressure and (b) EDS microanalysis spectrum for the region shown in the figure (a).

Table 5.2 – Chemical composition of the MgVAlCrNi alloy produced by HEBM under hydrogen pressure as measured by EDS.

at. %	Mg	V	Al	Cr	Ni
SEM	18.8±0.9	20.8±0.8	18.8±0.9	20.2±0.8	21.4±0.4

Figures 5.4a and 5.4b shows TEM bright field (BF) and dark field (DF) images, respectively, for a single particle of the MgVAlCrNi alloy produced by HEBM under hydrogen pressure. The sample present a crystallite size between 5 and 20 nm. The electron diffraction pattern (Figure 5.4c) confirms that only the BCC phase is present in this particle, which corroborates with the XRD results. Figure 5.5 shows STEM images of a single powder particle of the HEBM MgAlVCrNi alloy with EDS-chemical mapping. The STEM-EDS mapping carried out inside the red square region (see Figure 5.5a) shows that the five chemical elements are homogeneously distributed in the particle indicating that the HEBM procedure employed was successful to produce a highly homogenous alloy.

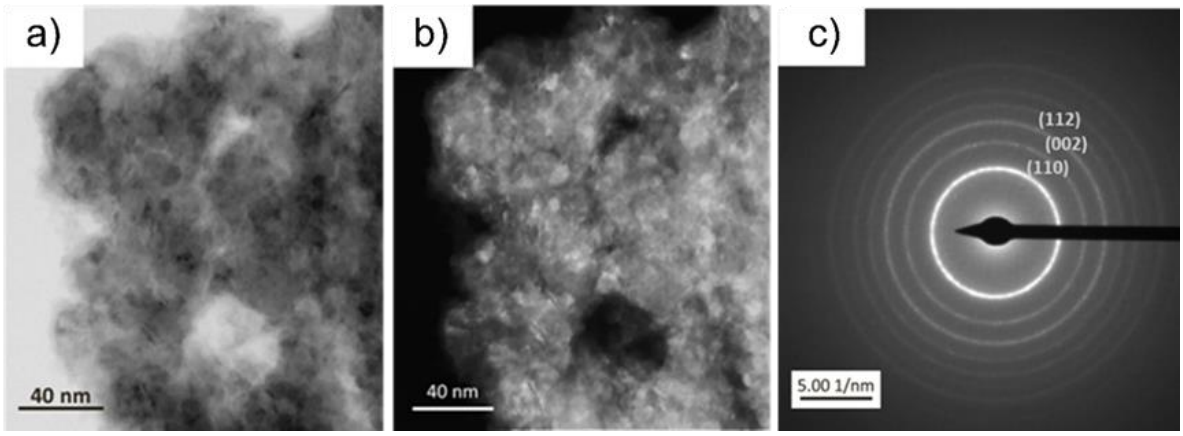

Figure 5.4 – TEM analysis of a single particle of the MgVAlCrNi alloy produced by HEBM under hydrogen pressure. (a) Bright field image, (b) dark field image and (c) electron diffraction pattern.

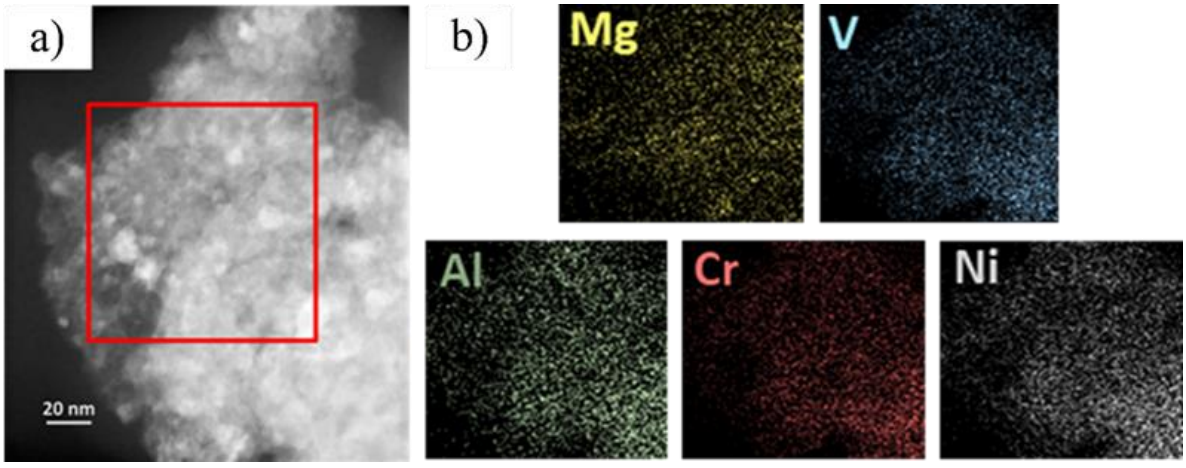

Figure 5.5 – (a) Dark field STEM image and (b) EDS mapping of a single particle of the MgVAlCrNi alloy produced by HEBM under hydrogen pressure. The red square indicates the area for EDS map acquisition**.**

Fig. 5.6 shows the XRD pattern of this alloy after DSC analysis. Only a single BCC phase is observed. A slight reduction of the BCC lattice parameter was observed, from the reactive milled sample to the desorbed sample (2.952(3) to 2.931(3) Å) which is related to the hydrogen releasing from the interstitial solid solution. This result shows that the BCC solid solution formed in the MgAlVCrNi alloy is very stable and do not decompose nor undergoes phase transformation when heated up to 550 º C. This is an important result, since elements can segregate, mainly magnesium. For example,

working with Mg-containing high entropy alloys, Marques et al. verified an important segregation of Mg from the disordered solid solution after heating under similar conditions [46].

To investigate whether the hydrogen pressure has an essential role in the phase formation during HEBM, the MgVAlCrNi alloy was also synthesized by HEBM under 0.7 MPa of argon. The XRD of the resulting alloy is also presented in Figure 5.6. Only a BCC phase with lattice parameter of a = 2.954(2) Å was formed for the sample produced by HEBM under argon pressure, which is similar to the sample synthesized under hydrogen pressure.

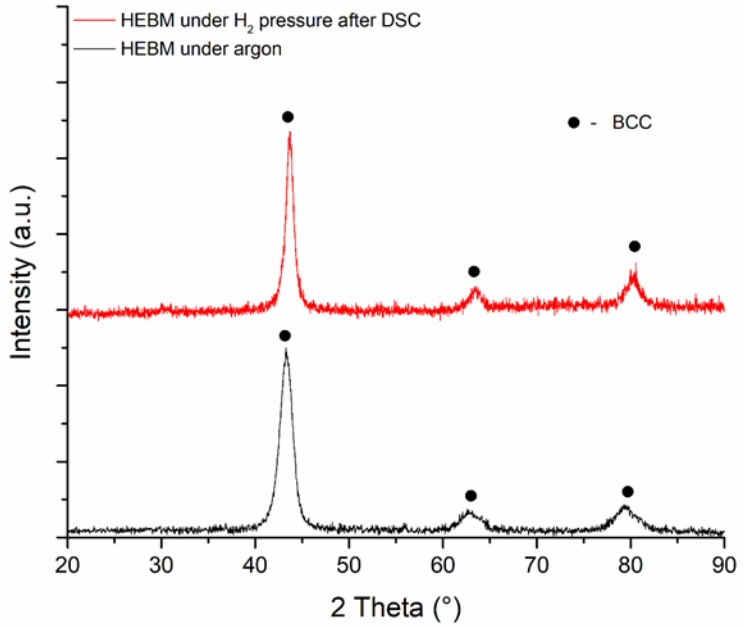

Figure 5.6 – XRD patterns of the MgVAlCrNi alloy produced by HEBM under argon pressure argon (black) and of the MgVAlCrNi alloy produced by HEBM under hydrogen pressure after DSC analysis (red).

Figure 5.7 shows the SEM micrograph of the sample of the MgVAlCrNi alloy synthesized by HEBM under argon pressure. Similarly to the sample produced under hydrogen pressure, this sample presented a heterogeneous particle size ranging from 0.5 to 15 µm and particle agglomerations. The chemical composition is close to the nominal composition as shown in Table 5.3.

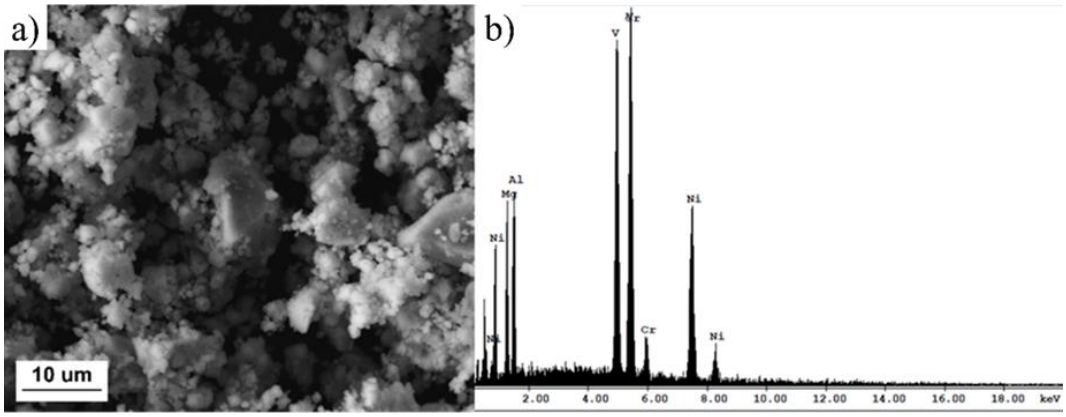

Figure 5.7 – SE-SEM micrograph of the MgVAlCrNi alloy produced by HEBM under 0.7 MPa of argon and (b) respective EDS spectrum.

Table 5.3 – SEM-EDS analysis of the MgVAlCrNi alloy produced by HEBM under 0.7 MPa of argon.

at. %	Mg	V	Al	Cr	Ni
SEM	18.5±0.3	20.9±0.3	18.0±0.3	21.2±0.5	21.4±0.5

Mg and Al contents were slightly lower than the nominal chemical composition regardless of the milling atmosphere. It is worth pointing out that no Mg or Al-rich particles were found. A possible explanation is the cold welding of Mg and Al with the milling tools. Mechanical alloying is a phenomenon of repeated cold welding and fracturing between powder particles. However, the use of soft materials, such as Al, and large particle sizes can promote more intense cold welding between the powder particles and vial walls / ball [48]. It is worth noting that the particle size of the starting Mg and Al powders were significantly larger than V, Cr, and Ni powders. Please, see the experimental details on session 4.1.2.

A comparison between both milling conditions shows that the small hydrogen content in solid solution in the sample prepared by HEBM under hydrogen pressure does not have a pronounced effect on the phase formation of the MgVAlCrNi alloy. Both milling conditions resulted in samples with a single BCC phase structure, similar powder morphology, and distribution of elements. The crystal density of the MgVAlCrNi alloy (considering the lattice parameter measured for the sample produced by HEBM under

argon atmosphere) is 5.48 g/cm³, which is comparable to the commercial Ti-based alloys (4.5–5 g/cm^3) and much lighter than Fe-based, Ni-based and refractory high entropy alloys [50,51]. Thus, the novel lightweight single-phase MgVAlCrNi HEA was successfully synthesized by HEBM.

As presented in Figure 5.2 (g), the equiatomic MgVAlNiCr alloy exhibited an endothermic event at 325°C related to hydrogen desorption (0.3 wt.%). The XRD measurements before and after the hydrogen desorption indicates a reduction of the lattice parameter, that represents a volume change of about 0.54 Å³ per unit cell. The volume of the unit cell per atom typically expands between 2 and 3 Å³ per hydrogen atom when hydrogen enters in solid solution in metal-hydrogen systems [52]. Therefore, it can be inferred that the number of hydrogen atoms per unit cell is between 0.18 and 0.27. This represents a hydrogen-to-metal ratio (H/M) between 0.09 and 0.135 and a gravimetric capacity between 0.208 wt.% and 0.313 wt.%., which agrees with the 0.3 wt.% mass loss detected by TGA measurement.

5.1.3 Structural characterization and hydrogen storage behavior of non-equiatomic Mg-V-Al-Cr-Ni HEAs

Two non-equiatomic alloys of the Mg-V-Al-Cr-Ni were designed to improve the hydrogen storage capacity. Three criteria were used for alloy design: the first criterion was to increase the fraction of Mg and V; the second criterion was increasing the alloy's lattice parameter. Usually, BCC HEA alloys that absorb a large amount of hydrogen has a lattice parameter higher than 3.00 Å. To achieve the second criterion, the mean atomic radius ($\bar{r}$) of the alloy was adjusted to be higher than the observed for the equiatomic alloy. Finally, the third criterion considered the Yang and Zhang semiempirical parameters for solid solution stabilization [8]. As seen previously in this work, even with δ values out of range (reference parameters: $\delta < 6.6\%$ and $\Omega > 1$), the equiatomic alloy crystalized in a BCC single phase. Therefore, the composition target was to obtain alloys that presented Ω values greater and δ values similar to the equiatomic alloy. Based on these criteria, the $Mg_{28}V_{28}Al_{19}Cr_{19}Ni_6$ and $Mg_{26}V_{31}Al_{31}Cr_6Ni_6$ alloys were proposed, and the calculated parameters are displayed in table 5.4.

Table 5.4 – Mean atomic radius, Ω and δ calculated from the nominal composition of the quinary alloys.

Alloy	Mean atomic radius (Å)	Ω	δ (%)
MgVAlCrNi	1.36	3.87	9.80
$Mg_{28}V_{28}Al_{19}Cr_{19}Ni_6$	1.40	4.73	9.90
$Mg_{26}V_{31}Al_{31}Cr_6Ni_6$	1.41	4.09	8.77

Fig 5.8a displays the XRD patterns of both quinary non-equiatomic alloys produced by HEBM under hydrogen pressure. For both compositions, the XRD patterns indicate the presence of a major BCC phase coexisting with another BCC phase (with smaller lattice parameter) and MgH_2. The samples were subjected to DSC analysis and were heated up to 550 °C. Fig. 5.8b shows the XRD patters of the sample after DSC analysis, which indicates that after hydrogen desorption, free Mg was observed as a result of the MgH_2 decomposition.

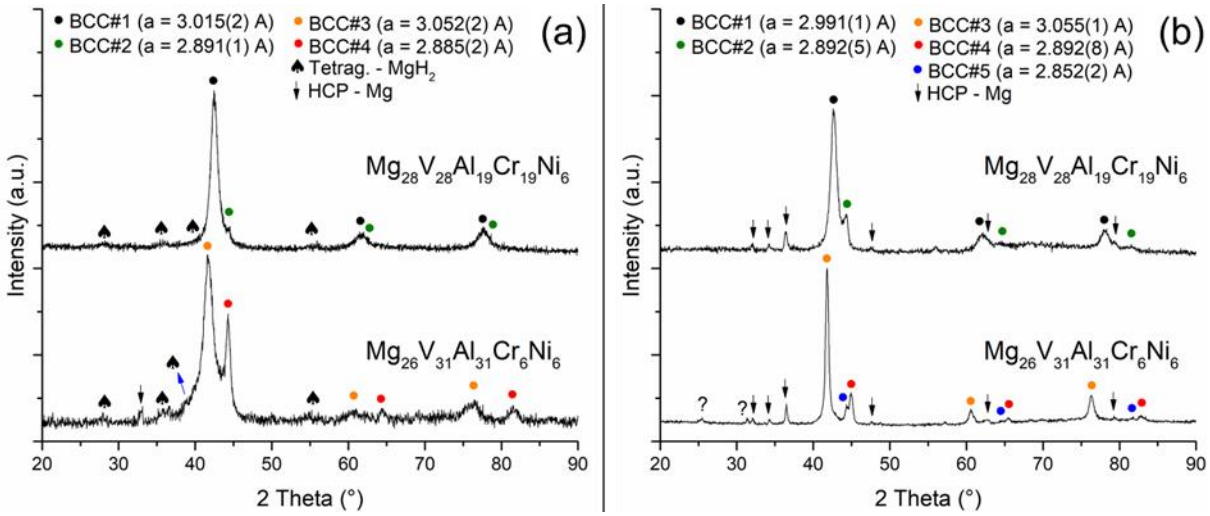

Figure 5.8 – Indexed XRD patterns of the non-equiatomic quinary alloys (a) after the HEBM process under 3.0 MPa of H_2 and (b) after DSC analysis.

For the $Mg_{28}V_{28}Al_{19}Cr_{19}Ni_6$, after hydrogen desorption, the lattice parameter of the major BCC phase decreases from 3.015(2) Å to 2.991(1) Å resulting in a volume variation of 0.64 $Å^3$. If this volume contraction is related to hydrogen desorption, this would represent a hydrogen-to-metal ratio (H/M) between 0.11 and 0.16 and a gravimetric capacity between 0.28 wt.% and 0.41 wt.%. The lattice parameter of the minor BCC phases did not change, indicating that this phase did not interact with hydrogen.

The XRD pattern of the $Mg_{26}V_{31}Al_{31}Cr_6Ni_6$ after DSC analysis displays three BCC phases. The lattice parameter of the major BCC phase remained the same as the as-milled condition. The minor BCC phase decomposes into two different BCC phases with lower relative intensity when compared to the minor BCC phase present in the as-milled condition.

Thus, for the equiatomic MgVAlCrNi alloy, the intrinsic features of the HEBM process combined with the entropic effect allowed the production of a highly homogeneous single-phase solid solution. However, a mixture of phases was observed for the compositions whose entropy is not maximized. Instead increase the hydrogen uptake of the major BCC, changing the alloy's stoichiometry leads to the formation of secondary phases and small fraction of magnesium hydride.

5.1.4 Discussion on the hydrogen storage behavior of HEAs from Mg-V-Al-Cr-Ni system

The above results indicate that regardless of the stoichiometry, the hydrogen capacity of the alloys of the Mg-V-Al-Cr-Ni system is low, even when the amount of hydride former elements, i.e., Mg and V, is increased. Therefore, the results suggest that the alloys of Mg-V-Al-Cr-Ni system have low affinity with hydrogen. The enthalpy of hydrogen solution and enthalpy of binary hydride formation of these alloying elements were analyzed to investigate reason of such low affinity with hydrogen. Table 5.5 shows the values of heating of solution and hydride formation for single elements.

As a strategy to improve the hydrogen storage capacity, the amount of Mg and V was increased because of the very negative standard enthalpy of formation of the MgH_2 (-37 kJ/mol H) and $VH_{0.5}$ (-42/-35 kJ/mol H). In the two non-stoichiometric alloys, Mg and V were more than 50 at.% of the alloy's composition. The original hypothesis was that increasing the fraction of strong hydride forming elements would improve the hydrogen affinity, but no significant improvement was observed. However, between the alloying elements, one can see that only V has a negative enthalpy of solution of hydrogen (-26 kJ/mol H), whereas all the other elements have very positive enthalpy of solution (Mg = +21 kJ/mol H, Al = +63 kJ/mol H, Cr = +28/+52 kJ/mol H, and Ni = +10/+24 kJ/mol H).

These values can explain the low hydrogen affinity in the alloys of the Mg-V-Al-Cr-Ni system.

Table 5.5 – Enthalpy of hydrogen solution (ΔH_∞) and formation of binary metal hydrides (ΔH_f^o) of the Mg-V-Al-Cr-Ni system. The concentrated hydrides are indicated in parenthesis. When two values are presented, they indicate the lowest and highest enthalpy values reported. Enthalpy values from ref. [53].

	Mg	**V**	**Al**	**Cr**	**Ni**
ΔH_∞ (kJ/mol H)	+21	-26	+63	+28 / +52	+10 / +24
ΔH_f^o (KJ/mol H)	-37 (MgH_2)	-42 / -35 ($VH_{0.5}$)	-4 (AlH_3)	-8 /+2 ($CrH_{0.5}$)	-3 ($NiH_{0.5}$)

The study of the Mg-V-Al-Cr-Ni system brought to light that the enthalpy of hydrogen solution of the alloying elements is also an important parameter to be considered in the design of hydrogen storage alloys. Table 5.6 shows the mean enthalpy of hydrogen solution ($\overline{\Delta H_\infty}$) and mean enthalpy of hydride formation ($\overline{\Delta H_f^o}$), calculated using equations 15 and 16, for different alloys reported in literature.

$$\overline{\Delta H_\infty} = \sum_{i=1}^{N}\{c_i(\Delta H_\infty)_i\} \quad (15)$$

$$\overline{\Delta H_f^o} = \sum_{i=1}^{N}\{c_i(\Delta H_f^o)_i\} \quad (16)$$

where $(\Delta H_\infty)_i$ is the enthalpy of hydrogen solution at infinite dilution and $(\Delta H_f^o)_i$ is the standard enthalpy of formation the concentrated hydride of element i. $(\Delta H_\infty)_i$ and $(\Delta H_f^o)_i$ values were taken from ref. [53].

As can be seen in table 5.6, the BCC HEAs with high hydrogen capacity, therefore, with high hydrogen affinity, have both highly negative values of $\overline{\Delta H_\infty}$ and $\overline{\Delta H_f^o}$, such as for the TiVNbZr, $Ti_{0.2}V_{0.2}Nb_{0.2}Zr_{0.4}$, TiVNbTa and TiZrNbHfTa alloys. Although having negative $\overline{\Delta H_f^o}$ values (comparable to that of TiVCrMo alloy, for instance), the MgVAlCrNi, $Mg_{28}V_{28}Al_{19}Cr_{19}Ni_6$ and $Mg_{26}V_{31}Al_{31}Cr_6Ni_6$ alloys have positive values of $\overline{\Delta H_\infty}$, which yield low affinity with hydrogen.

One of this work's strategies to increase the alloy's hydrogen storage capacity was to use Al (a lightweight element) to reduce its weight. Unfortunately, the enthalpy of hydrogen solution in aluminum is amongst the highest ones in the periodic table. Only Si,

Sn, W and Ir have a hydrogen enthalpy of solution higher than Al [53]. Besides that, unlike the transition metals usually employed in BCC HEA for hydrogen storage such as Ti, V, Nb, Zr, Ta and Hf, magnesium also has a very positive enthalpy of hydrogen solution while having a very negative enthalpy of formation of its hydride (MgH_2). These positive enthalpies of hydrogen solution make the Mg and Al-containing HEAs' design for hydrogen storage even more challenging.

Table 5.6 – Hydrogen uptake, hydride crystal structure, calculated mean enthalpy of solution ($\overline{\Delta H_\infty}$) and mean enthalpy of hydride formation ($\overline{\Delta H_f^o}$) of different BCC HEAs reported in the literature. $(\Delta H_\infty)_i$ and $(\Delta H_f^o)_i$ values were taken from ref. [53].

Alloy	**Hydrogen uptake (H/M)**	**Hydride struct.**	**ΔH_∞ (kJ/mol H)**	**ΔH^o (KJ/mol H)**	**[Ref.]**
TiVZrNbHf	2 - 2.5	BCT	-43.6	-59.0	[18,19]
TiVNbZr	1.7	BCT	-45.0	-57.2	[43]
$Ti_{0.2}V_{0.2}Nb_{0.2}Zr_{0.4}$	~ 2	FCC	-48.8	-62.2	[38]
TiVNbTa	~ 2	FCC	-38.0	-46.2	[38]
TiZrHfMoNb	~ 1.2	FCC	-31.6	-51.0	[54]
TiZrNbHfTa	~ 2	FCC	-45.6	-59.6	[16]
$Mg_{21}Ti_{31}Nb_{31}Ni_{17}$	~ 1	FCC	-21.8	-43.0	[46]
$Mg_{0.22}Ti_{0.22}Zr_{0.22}Fe_{0.11}Co_{0.11}Ni_{0.11}$	~ 0.7	BCC + FCC	-14.4	-39.11	[45]
AlCrFeMnNiW	-	BCC	+11	-7.6	[42]
TiVCrMo	~ 0.7	BCC	-4	-26	[39]
MgVAlCrNi	~ 0.15	BCC	+12.2	-17	This work
$Mg_{28}V_{28}Al_{19}Cr_{19}Ni_6$	~ 0.15	BCC	+9.84	-22.24	This work
$Mg_{26}V_{31}Al_{31}Cr_6Ni_6$	-	BCC	+8.36	-22.25	This work

5.2 Design of single BCC HEA from the Mg-Al-Ti-Mn-Nb system

This section presents a semiempirical approach to design single BCC Mg-containing HEAs for hydrogen storage. The new design method was applied to the Mg-Al-Ti-Mn-Nb system to select a composition with high tendency to form single BCC solid solution with high hydrogen affinity.

5.2.1 Alloy design

The design approach proposed here is based on four criteria. Firstly, φ is set to be higher than 20, so single-phase solid solution formation is more likely to occur. Second, VEC is set to be lower than 6.87 to have BCC structure. Finally, considering the discussed content in session 5.1.4, the hydrogen affinity is assessed by setting $\overline{\Delta H_{\infty}}$ and $\overline{\Delta H_f^o}$ to negative values. In this work, $\overline{\Delta H_{\infty}}$<$-20$ kJ/mol of H and $\overline{\Delta H_f^o}$<-40 kJ/mol of H was set as targets. The method was applied to the Mg-Al-Ti-Nb-Mn system. By grouping the elements with positive values of ΔH_{∞} (Al and Mn) and the elements with negative values of ΔH_{∞} (Ti and Nb), the four parameters were calculated for 1326 compositions with $(TiNb)_x(AlMn)_yMg_{1-x-y}$ stoichiometry. Table 5.7 presents the data necessary to calculate the four parameters.

Table 5.7 – Data used to calculate the φ, VEC, $\overline{\Delta H_{\infty}}$ and $\overline{\Delta H_f^o}$ for the M-Al-Ti-Mn-Nb system. Atomic radii (r) and melting point of the pure elements were taken from [12]. The VEC values were taken from [10]. The enthalpy of mixing for the binary systems (ΔH_{mix}^{ij}) [29]. The values of ΔH_{∞} and ΔH_f^o were taken from [53].

Element i	r (Å)	ΔH_{mix}^{ij} (kJ/mol)				Tm (K)	VEC	ΔH_{∞} (kJ/mol H)	ΔH_f^o (kJ/mol H)
		Al-j	Ti-j	Mn-j	Nb-j				
Mg	1.601	-2	16	10	32	923	2	+21.0	-37.0
Al	1.432	-	-30	-19	-18	933	3	+28.0	-4.0
Ti	1.462	-	-	-8	2	1941	4	-52.0	-68.0
Mn	1.350	-	-	-	-4	1519	7	+1.0	-8.0
Nb	1.429	-	-	-	-	2750	5	-38.0	-44.0

The calculated parameters are presented in Figure 5.9 in the form of ternary diagrams. Note that AlMn and TiNb share the diagrams' vertices. The white star in Figure 5.9 indicates the selected composition $Mg_{12}Al_{11}Ti_{33}Mn_{11}Nb_{33}$, which is inside the compositional field that meets the four design criteria delimited by the dashed line in Fig. 5.9(a). This alloy was selected because it is the alloy in this field that contains the highest amount of the lightweight elements, Mg and Al. The black star in Figure 5.9 indicates the equiatomic alloy, which is outside the field of interest. Table 5.8 shows the values of the four parameters for both $Mg_{12}Al_{11}Ti_{33}Mn_{11}Nb_{33}$ and $Mg_{20}Al_{20}Ti_{20}Mn_{20}Nb_{20}$ compositions. Both alloys were produced for comparison.

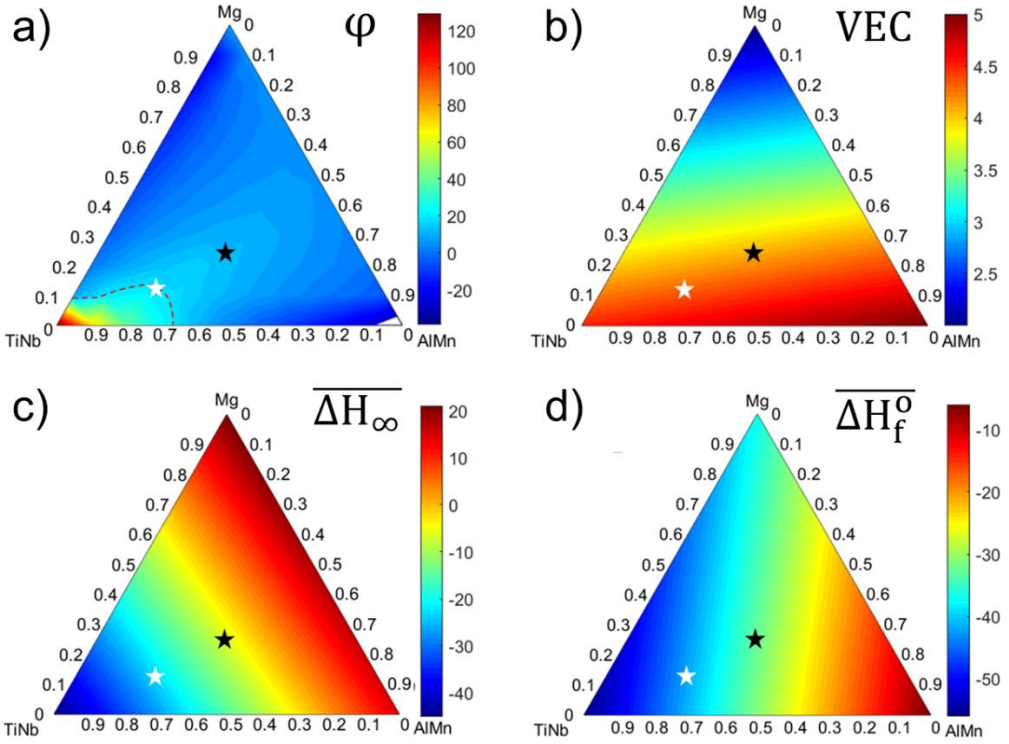

Figure 5.9 – Calculated parameters for the $(TiNb)_x(AlMn)_yMg_{1-x-y}$ system. (a) φ. The dashed line indicates the compositions with $\varphi = 20$, (b) VEC, (c) $\overline{\Delta H_\infty}$ (kJ/mol H) and (d) $\overline{\Delta H_f^o}$ (kJ/mol H). Black star corresponds to the equiatomic alloy; white star indicates the selected $Mg_{13}Al_{11}Ti_{33}Mn_{11}Nb_{33}$ alloy.

Table 5.8 –Calculated parameters for the select compositions.

Alloy	φ	VEC	$\overline{\Delta H_\infty}$ (kJ/mol H)	$\overline{\Delta H_f^o}$ (kJ/mol H)
$Mg_{12}Al_{11}Ti_{33}Mn_{11}Nb_{33}$	20.7	4.31	-24.0	-42.7

$Mg_{20}Al_{20}Ti_{20}Mn_{20}Nb_{20}$.	12.1	4.20	-8.0	-32.2

5.2.2 Synthesis and characterization of the equiatomic and designed alloys

Figure 5.10 exhibits the XRD patterns of the synthesized alloys. The XRD pattern of $Mg_{12}Al_{11}Ti_{33}Mn_{11}Nb_{33}$ was indexed as a single-phase BCC with a lattice parameter a = 3.238(1) Å. Values in parenthesis are uncertainties on the last significant digit. No additional diffraction peaks were observed. The XRD pattern of the $Mg_{20}Al_{20}Ti_{20}Mn_{20}Nb_{20}$ alloy reveals a mixture of phases. The most intense diffraction peaks seem to belong to a BCC structure, and diffraction peaks of α-Mn are observed. Furthermore, a broad peak between 33° and 45° overlapped with the 110 reflection of the BCC phase can be observed. Such broad peak may result either from some fraction of the amorphous phase or the convolution of unidentified phase reflections.

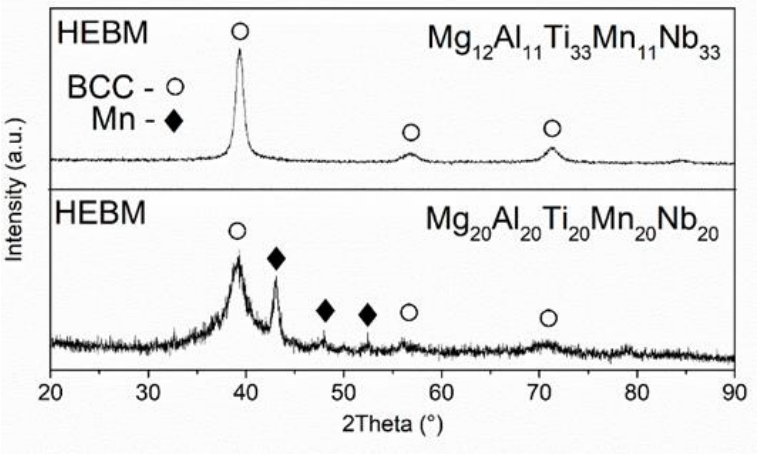

Figure 5.10 – XRD patterns of the $Mg_{12}Al_{11}Ti_{33}Mn_{11}Nb_{33}$ and $Mg_{20}Al_{20}Ti_{20}Mn_{20}Nb_{20}$ alloys produced by HEBM under argon atmosphere.

To check the structural and chemical homogeneity of the $Mg_{12}Al_{11}Ti_{33}Mn_{11}Nb_{33}$ alloy, a more in-depth structural characterization was carried out. Figure 5.11 shows the SEM images for the milled powder. As seen by the SE-SEM image (figure 5.11 (a)), the powder's morphology consisted of round particles of various particle size. No apparent segregation of the elements was observed from a high magnification backscattered electron micrography of the powder (Fig. 5.11 (b)).

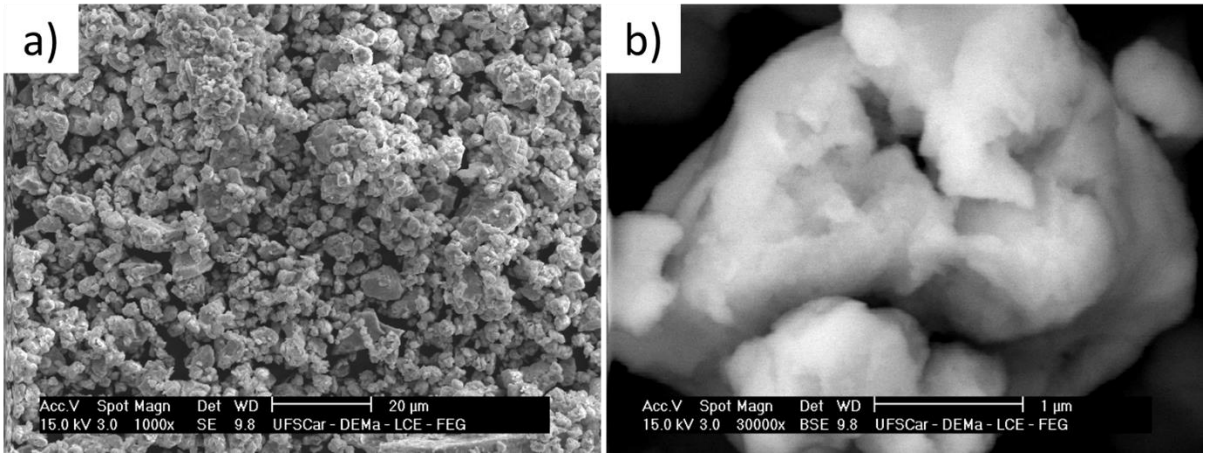

Figure 5.11 – SEM images of the $Mg_{12}Al_{11}Ti_{33}Mn_{11}Nb_{33}$ alloy after synthesis by HEBM under argon atmosphere. (a) Secondary-electrons image and (b) Backscattered-electron image.

Figure 5.12 shows TEM images of the as-milled $Mg_{12}Al_{11}Ti_{33}Mn_{11}Nb_{33}$. The dark-field image (Figure 5.12 (b)) reveals a nanocrystalline structure evidenced by the crystallites at the edge (thinner area) of the powder particle. Figure 5.12 (d) and (e) show a STEM BF image and its corresponding EDS elemental mapping, respectively, and indicates that the five alloying elements are homogeneously distributed in the particle. Table 5.9 shows the composition measured by TEM-EDS analysis (Figure 5.12) and compares it with the mean composition determined by SEM-EDS from 10 random particles. The measured composition is in good agreement with the nominal one. The electron diffraction pattern of a single particle presented in Figure 5.12 (c) was also indexed as a single BCC phase.

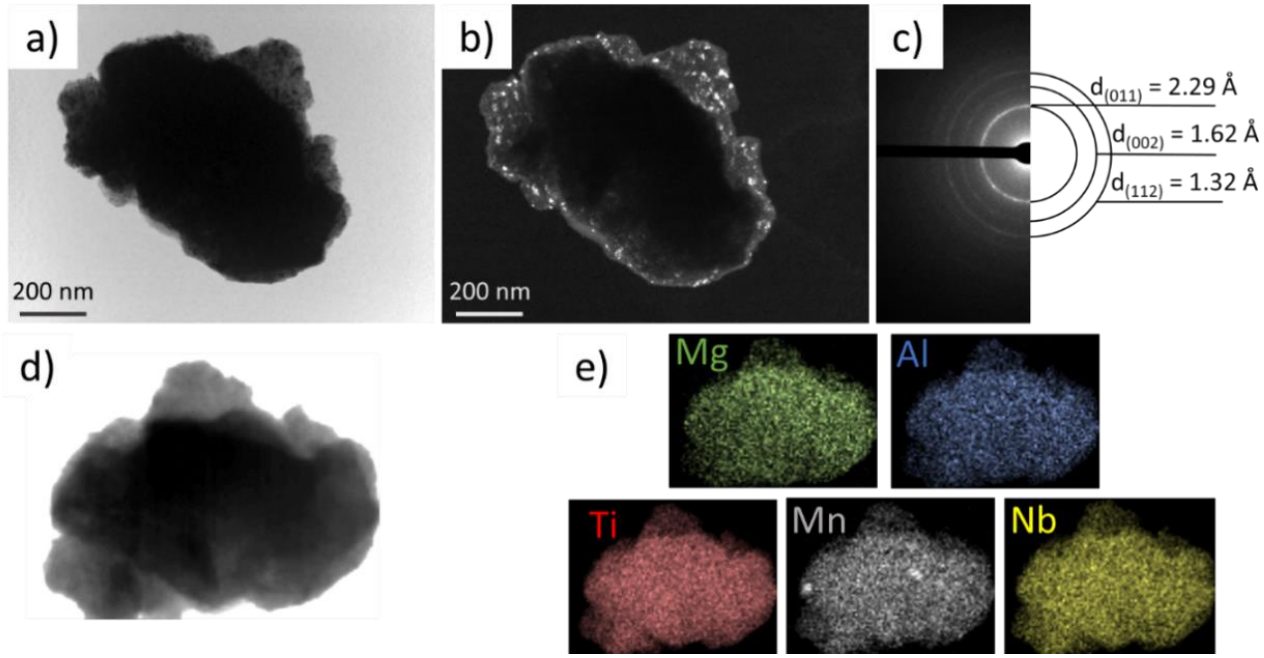

Figure 5.12 – TEM characterization of as-milled $Mg_{12}Al_{11}Ti_{33}Mn_{11}Nb_{33}$ powder. (a) Bright-field image, (b) dark-field image acquired using the 011-reflection ring, and (c) indexed electron diffraction pattern. (d) bright-field STEM image and (e) EDS mapping of a single particle.

Table 5.9 – Chemical composition (at.%) of the $Mg_{12}Al_{11}Ti_{33}Mn_{11}Nb_{33}$ alloy produced by HEBM under argon atmosphere measured by EDS.

	Mg	**Al**	**Ti**	**Mn**	**Nb**
Nominal	12.0	11.0	33.0	11.0	33.0
TEM	8.9(4)	8.4(4)	35(1)	11.7(9)	36(3)
SEM	10.6(1)	9.9(3)	34.7(3)	9.6(1)	35.1(3)

The equiatomic alloy has $\varphi = 12$, and the XRD result shows that this alloy is not a single phase. On the other hand, the $Mg_{12}Al_{11}Ti_{33}Mn_{11}Nb_{33}$ processed under the same conditions is a single-phase alloy. These results agree with the tendency proposed by Ye et al., which state that above the critical $\varphi_{crit} = 20$ the sample tends to be a solid solution [12]. Therefore, $\varphi > 20$ was successfully applied for designing single-phase alloys. Since the equiatomic alloy is not a single phase, only the hydrogen storage properties of the $Mg_{12}Al_{11}Ti_{33}Mn_{11}Nb_{33}$ alloy were evaluated in this work.

5.2.3 Hydrogen storage behavior od the $Mg_{12}Al_{11}Ti_{33}Mn_{11}Nb_{33}$ alloy

Figure 5.13 (a) shows the pressure-composition-isotherm (PCI) measured at 275°C for the $Mg_{12}Al_{11}Ti_{33}Mn_{11}Nb_{33}$ alloy. Initial kinetic measurements (omitted here) under different temperatures and hydrogen pressure (30 bar) indicated that the lower temperature at which absorption occurs was found to be 275ºC. As shown in Figure 5.13 (a), the maximum hydrogen absorption capacity was about 1.75 wt.% (H/M=1.05). XRD measurement after the PCI test (figure 5.13 (b)) shows that only an expanded BCC phase with a=3.372(1) Å is present in the hydrogenated sample. This corresponds to a volume expansion of 4.6 Å³ per unit cell. According to the Peisl relationship, the unit cell volume varies from 2 to 2.9 Å³ per absorbed hydrogen atom [52]. Therefore, the estimated number of hydrogen atoms per unit cell is between 1.6 and 2.3, representing a H/M between 0.8 and 1.1, in agreement with the measured hydrogen uptake. Desorption measurements were carried out by coupled thermal analysis. The results presented in Figure 5.13(c) show that the hydrogen desorption starts at approximately 300°C and is complete at 520°C. The mass loss detected by TGA was about 1.75 wt.%, meaning a complete de-hydrogenation. Despite the hydrogenated sample presenting a single BCC phase, two overlapped endothermic peaks related to hydrogen desorption could be seen in the DSC curve. XRD measurement after thermal analysis demonstrates that the original BCC phase is restored after complete desorption (a=3.239(7) Å), and no second phases are formed (Figure 5.13 (b)).

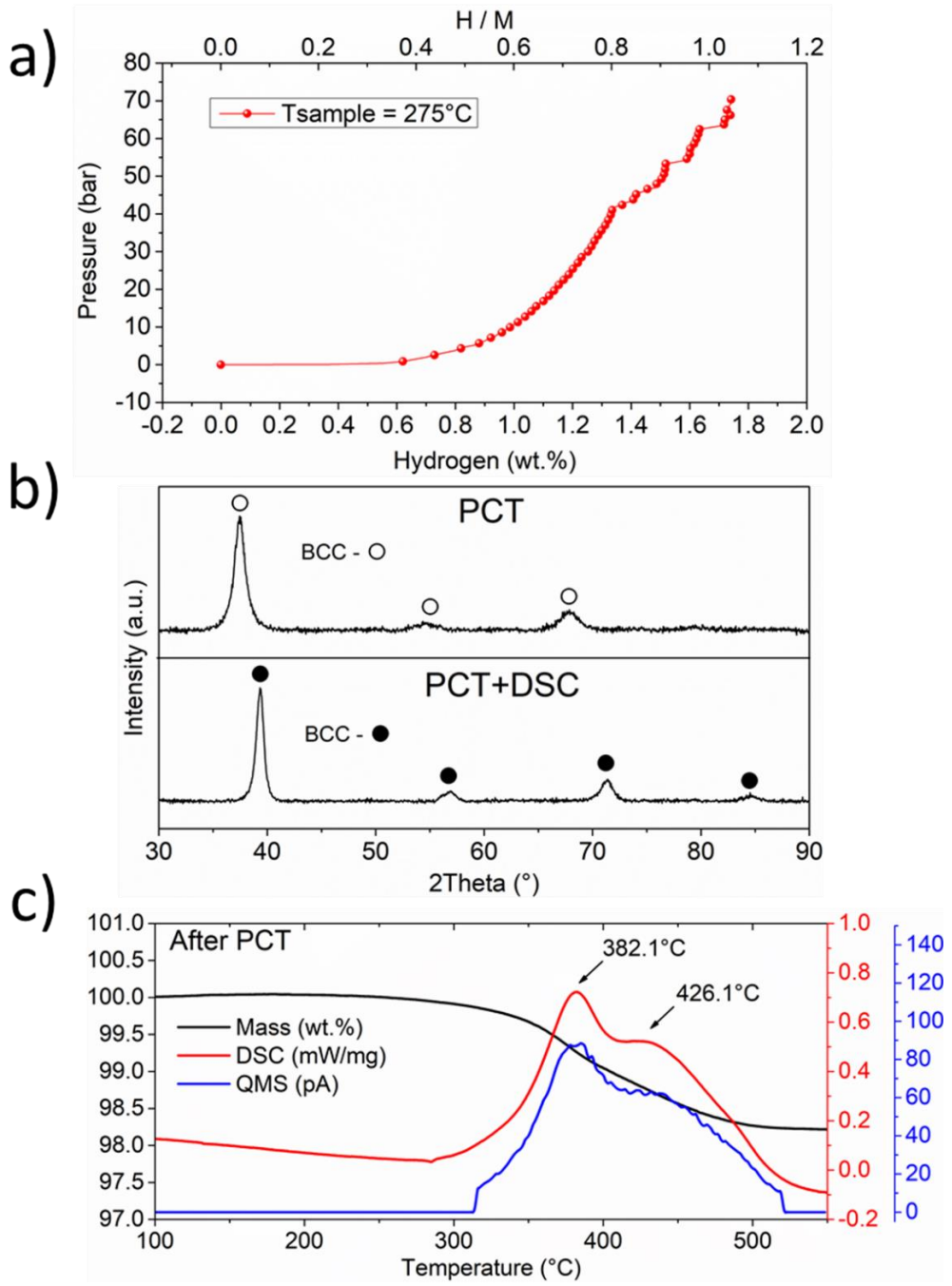

Figure 5.13 – PCI absorption isotherm at 275°C of the $Mg_{12}Al_{11}Ti_{33}Mn_{11}Nb_{33}$ alloy. (b) XRD pattern after PTC and after DSC measurements. (c) DSC, TGA and QMS (H_2 signal) curves of $Mg_{12}Al_{11}Ti_{33}Mn_{11}Nb_{33}$ after PCI measurement.

5.2.4 Characterization of $Mg_{12}Al_{11}Ti_{33}Mn_{11}Nb_{33}$ produced by reactive milling

Reactive HEBM is a suitable process route to prepare metal hydrides. Thus, the $Mg_{12}Al_{11}Ti_{33}Mn_{11}Nb_{33}$ alloy was also produced by reactive milling under 30.0 bar of H_2. Figure 5.14 (a) shows the XRD patterns of the $Mg_{12}Al_{11}Ti_{33}Mn_{11}Nb_{33}$ alloy prepared by the reactive milling. The XRD data could be indexed as CaF_2-type face-centered cubic structure (FCC hydride) with a lattice parameter of a = 4.54(3) Å. The peak broadening is related to the crystal structure imperfections and the crystallite size [55]. The hydrogen desorption was evaluated by thermal analysis (Figure 5.14 (b)). The DSC was carried out with the same conditions as the ball-milled under argon atmosphere powder after absorption, e.g., 10 ºC min^{-1} and an argon flow of 50 mL min^{-1}. However, the desorption profile shows a main endothermic peak with a maximum desorption rate at around 324°C, immediately followed by the appearance of a shoulder, which can be interpreted as a second overlapped peak. The DSC profile indicates that the hydrogen desorption starts at approximately 210°C and is complete at 520°C. The QMS curve follows the DSC profile, indicating dehydrogenation. The estimated mass loss detected by TGA was also about 1.75 wt.%, which indicates a theoretical hydrogen uptake of about H/M=1. After the DSC analysis, the crystal structure undergoes a phase transformation to a BCC with lattice parameter a = 3.27(2) Å, similarly to the phase observed after HEBM under argon atmosphere (a = 3.238(1) Å).

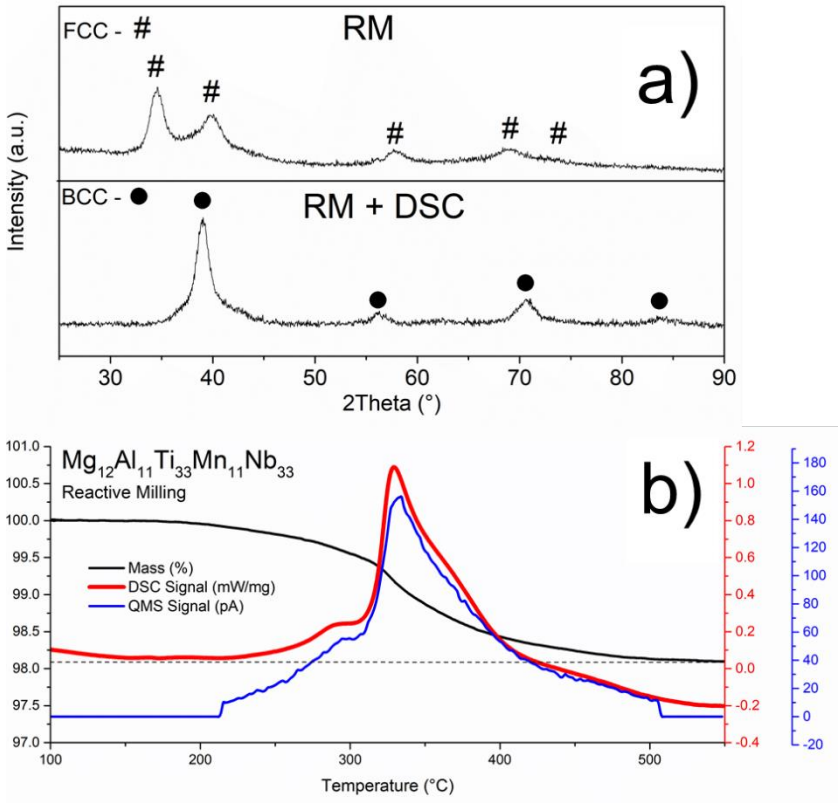

Figure 5.14 – (a) XRD pattern of the $Mg_{12}Al_{11}Ti_{33}Mn_{11}Nb_{33}$ after reactive milling and after DSC analysis. (b) Hydrogen desorption measured by DSC analysis, where the QMS signal is related to the H_2 release.

The above results indicate few differences between the hydrides of the $Mg_{12}Al_{11}Ti_{33}Mn_{11}Nb_{33}$ alloy processed by HEBM under argon and hydrogenated by volumetric techniques and the hydride produced by reactive milling. The difference between the DSC peak profiles can be explained in terms of kinetics. According to Montero et al. the direct synthesis of metal hydrides by reactive ball milling of metallic constituents, allows the preparation of hydrides with better kinetics of desorption than the hydrogenated powders produced by high energy ball milling under inert atmosphere [43]. The shifted peaks to lower temperatures for the reactive milled powder evidence this. As shown, both alloys release the same amount of hydrogen, but the hydride crystal structure is not identical. Despite the high pressure applied during the hydrogen absorption of the $Mg_{12}Al_{11}Ti_{33}Mn_{11}Nb_{33}$ alloy (275ºC under 70 bar of H_2), an FCC structure was not formed, while the reactive ball milled powder exhibit the CaF_2 FCC structure. For BCC alloys, the phase transformation at hydrogenation (BCC to FCC) occurs for hydrides containing a

hydrogen uptake around H/M=1.1 [56]. However, the FCC structure is only achieved by reactive mechanical alloying [49]. Surprisingly, the H desorption capacities measured by thermal analysis of the BCC and FCC hydrides of the $Mg_{12}Al_{11}Ti_{33}Mn_{11}Nb_{33}$ alloy were very close to each other. The reason for this phenomenon is not clear yet and deserves further investigation.

5.2.5 Discussion on the hydrogen storage behavior of the $Mg_{12}Al_{11}Ti_{33}Mn_{11}Nb_{33}$ HEA

Table 5.10 shows the values of $\overline{\Delta H_{\infty}}$, $\overline{\Delta H_f^o}$ and the hydrogen uptake for some BCC HEAs. For alloys that achieved H/M~2, such as TiVNbZrHf, TiZrNbHfTa and TiVNbTa, it is possible to see that both quantities are very negative, i.e., around -40 kJ/mol H. The value of $\overline{\Delta H_f^o}$ for the $Mg_{12}Al_{11}Ti_{33}Mn_{11}Nb_{33}$ is lower than -40 kJ/mol H while the value of $\overline{\Delta H_{\infty}}$ is only -24 kJ/mol H because the ΔH_{∞} of magnesium is very positive (+21 kJ/mol of H). From Table 5.10, one can see that this trend repeats for other Mg-containing HEAs, an indication that balancing the alloy elements to reduce the values of $\overline{\Delta H_{\infty}}$ and $\overline{\Delta H_f^o}$ is crucial to increase the hydrogen storage capacity of the alloy.

Figure 5.9 (c) shows that the only compositional region of the Mg-Al-Ti-Mn-Nb system where $\overline{\Delta H_{\infty}} < -40$ kJ/mol H can be achieved is at the TiNb vertex. In this case, the lightweight effect of Mg and Al on the gravimetric capacity would disappear. It is worth noting that, due to its lightweight, even forming a monohydride, the gravimetric capacity of the $Mg_{12}Al_{11}Ti_{33}Mn_{11}Nb_{33}$ alloy is still competitive with other refractory HEAs that formed dihydrides. For example, TiZrNbHfTa and TiVZrNbTa can achieve H/M~2, which corresponds to gravimetric capacities of 1.7 and 1.8 wt.%, respectively. This is approximately the same capacity as the $Mg_{12}Al_{11}Ti_{33}Mn_{11}Nb_{33}$ alloy with H/M~1 (1.75 wt.%). Moreover, the gravimetric capacity of this alloys is significantly higher than some BCC alloys, which combine hydride forming and non-hydride forming elements such as e.g., MgAlVCrNi (Session 5.1), TiVCrMo [39] and TiVNbCrMo [39].

Table 5.10 – Hydrogen uptake, $\overline{\Delta H_{\infty}}$ and $\overline{\Delta H_f^o}$ for different Mg-containing alloys. The values of ΔH_{∞} and ΔH_f^o for each element were taken from [53].

Alloy	**Hydrogen uptake (H/M)**	$\overline{\Delta H_{\infty}}$ **(kJ/mol H)**	$\overline{\Delta H_f^o}$ **(kJ/mol H)**	**Ref.**
TiZrNbHfTa	~2	-38.0	-50.0	[16,17]
TiVNbZrHf	~2	-43.6	-59.0	[18,19]
TiVNbTa	~2	-38.0	-46.0	[38]
MgVAlCrNi	~0.15	+12.2	-17.0	Session 5.1
MgTiVCrFe	~0.13	0	-27.12	[57]
$Mg_{22}Ti_{22}Zr_{22}Fe_{11}Co_{11}Ni_{11}$	~0.7	-14.4	-39.11	[45]
$Mg_{21}Ti_{31}Nb_{31}Ni_{17}$	~1	-21.8	-43.0	[46]
$Mg_{12}Ti_{33}Al_{11}Mn_{11}Nb_{33}$	~1.1	-26.5	-44.1	This work

5.3 Design of BCC HEA for hydrogen storage by CALPHAD: Addition of non-hydride forming element to the Ti-V-Nb system

In this section, a well-known ternary hydride was selected, and the effects of the addition of a non-hydride forming element were investigated. CALPHAD method was used as a design tool to select the non-hydride forming element that could be added to the system at different levels without resulting in the formation of second phases. Therefore, three alloys with different fraction of the selected element were produced and their hydrogen storage properties were evaluated. The final goal was to design a quaternary alloy system with tunable H storage properties.

5.3.1 Alloy design

Figure 5.15 displays the thermodynamic calculation carried out by CALPHAD method, where the amount of equilibrium phases is plotted as a function of temperature. As seen in figure 5.15 (a), the ternary TiVNb alloy predictions exhibit a large BCC single-phase field at high temperatures and no secondary phases appear even at low temperatures, which agrees with the initial objective of this work. The addition of different non-hydride forming elements in this ternary system was also investigated by CALPHAD. The equilibrium phases as function of temperature were calculated for the equiatomic quaternary TiVNbM (M = Cr, Mn, Fe, Co, Ni) alloys (Figure 5.15 (b) to (f)). One can see that only the TiVNbCr exhibits a large BCC single-phase field. The other alloys' equilibrium phases are composed mainly of secondary BCC phases, differing from each other by the composition and ordered phases as the Laves type phases. Therefore, the quaternary $(TiVNb)_{100-x}Cr_x$ was taken as the basis for this project.

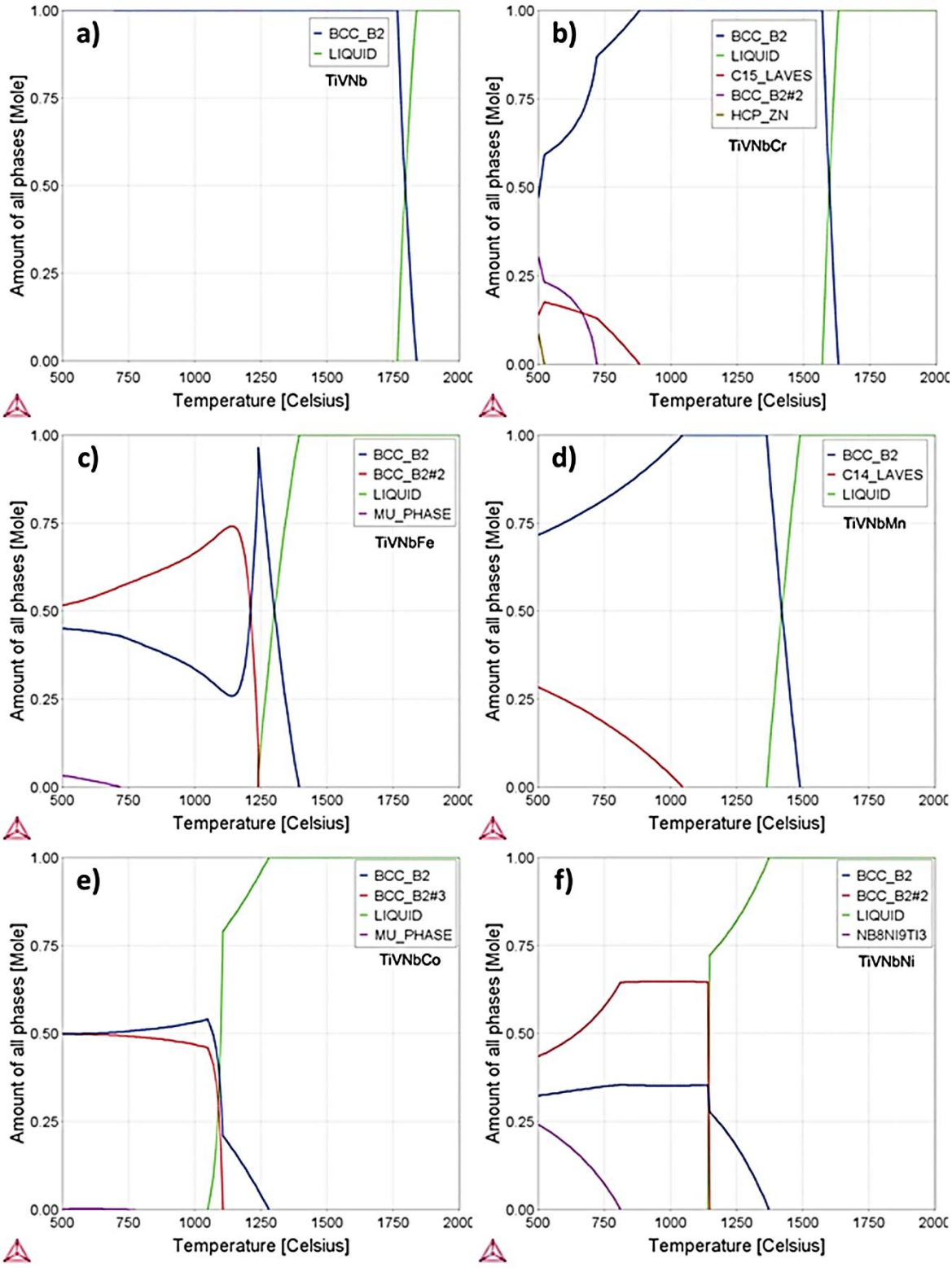

Figure 5.15 – Thermodynamic calculation of the TiVNbM (M = Cr, Mn, Fe, Co and Ni) system. Amount of equilibrium phases against temperature. TiVNb (a), TiVNbCr (b), TiVNbCr (c), TiVNbFe (d), TiVNbCo (e) and, TiVNbNi (f).

Since the goal of this work was to obtain a BCC solid solution by varying the fraction of the non-hydride forming element, the equilibrium phases as a function of temperature were calculated for three compositions: $(TiVNb)_{85}Cr_{15}$, $(TiVNb)_{75}Cr_{25}$ and $(TiVNb)_{65}Cr_{35}$. As can be seen figure 5.16, when Cr is added, the formation of a C15-type Laves phase at low temperature is predicted. As the Cr content increases, the temperature of formation of C15-Laves phase also increases. However, the thermodynamic calculations show that a large BCC single-phase field at high temperatures are present for the three alloys, making them excellent candidates for this project.

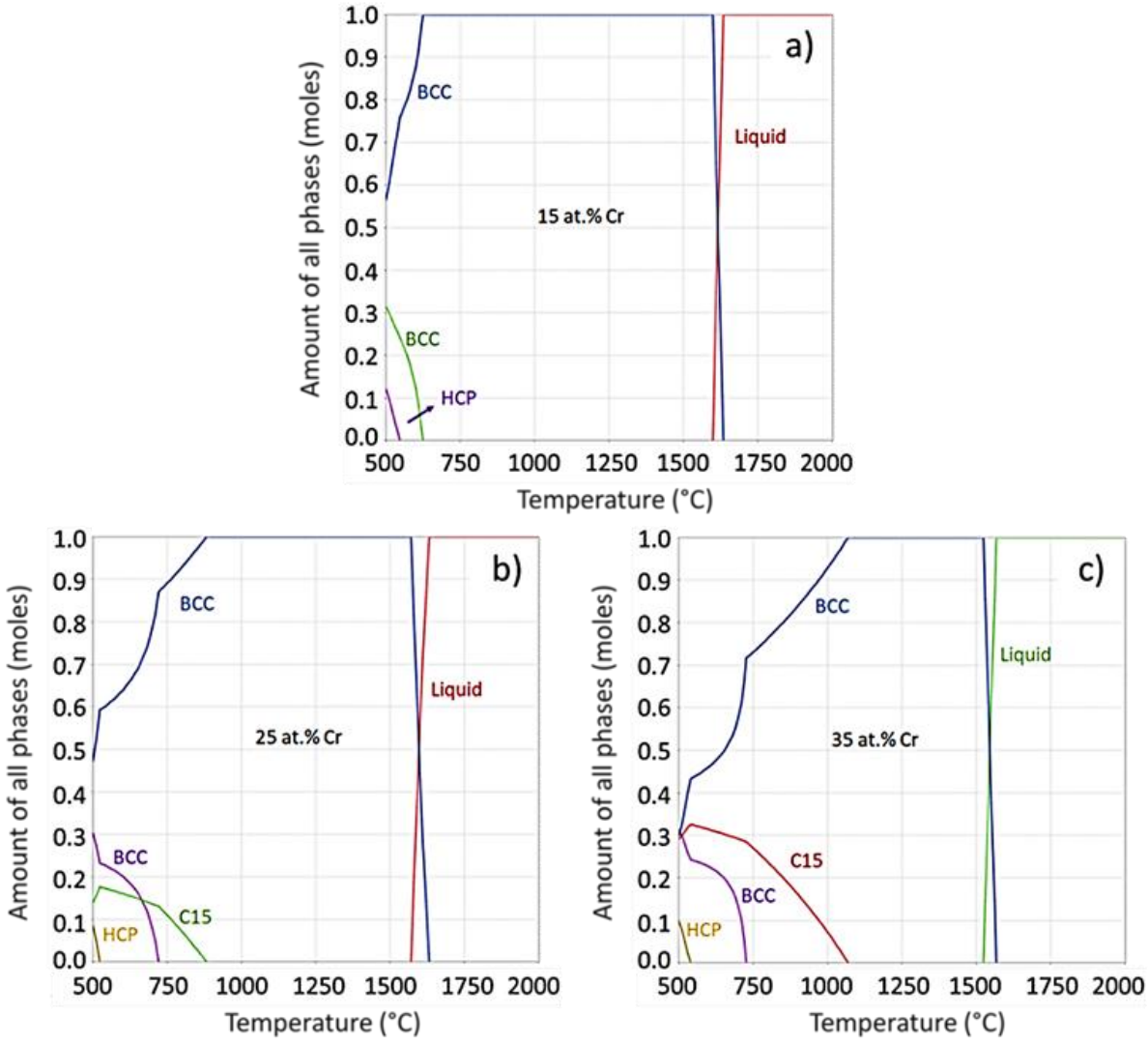

Figure 5.16 – CALPHAD thermodynamic calculation of $(TiVNb)_{100-x}Cr_x$ alloys. Amount of equilibrium phases as a function of temperature. x = 15 (a), (b) x = 25 and (c) x = 35 at.% Cr.

5.3.2 Structural characterization

The microstructure of the arc-melted ingots was investigated by SEM and the backscattered electron micrographs of the alloys are shown in figure 5.17. EDS measurements were carried out to investigate the composition, and the yellow arrows on the micrograph indicate representative EDS points for each phase. The average measured composition of each phase is shown in Table 5.11. The arc melted samples are composed of a dendritic matrix. The contrast difference between the dendrite core (bright gray) and boundaries (dark gay) reveals a composition gradient. The dendrite's center tends to be niobium rich and the dark gray regions are Cr and Ti-rich. The composition gradient comes from Ti and Cr segregation. As seen in Table 5.11, the bright and dark gray phases' chemical compositions are relatively close. For the samples containing 15 and 25 at.% Cr, associated with this segregation is the formation of a black phase. As seen in Table 5.11, this phase is titanium-rich precipitate.

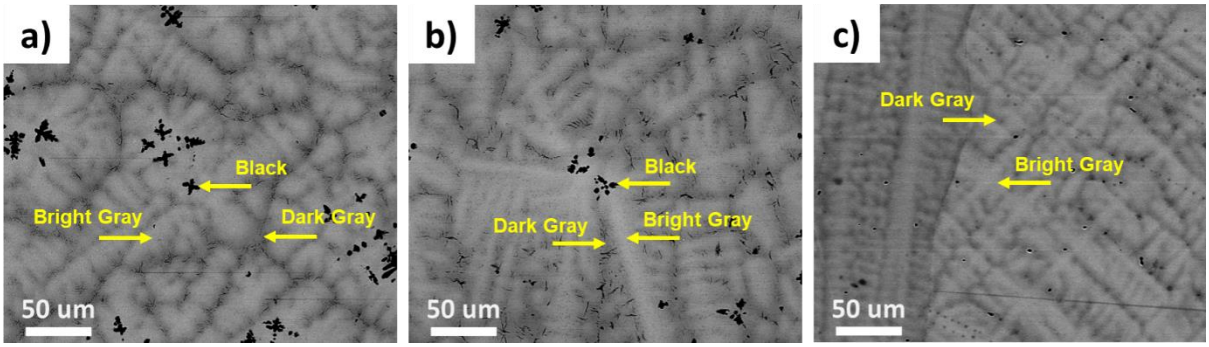

Figure 5.17 –Backscattered electron micrograph of as-cast alloys: $(TiVNb)_{85}Cr_{15}$ (a), $(TiVNb)_{75}Cr_{25}$ (b) and $(TiVNb)_{65}Cr_{35}$ (c).

Table 5.11 – Average EDS measured composition. The yellow arrows indicated in figure 5.17 are representative points for each region.

	Composition for each alloy in the as-cast condition (at. %)							
	$(TiVNb)_{85}Cr_{15}$			**$(TiVNb)_{75}Cr_{25}$**			**$(TiVNb)_{65}Cr_{35}$**	
	Bright Gray	**Dark Gray**	**Black**	**Bright Gray**	**Dark Gray**	**Black**	**Bright Gray**	**Dark Gray**
Ti	28.0 (3)	29.5 (8)	88.5 (4)	22.9 (3)	24.9 (4)	89.0 (2)	22.8 (5)	25 (1)
V	30.6 (3)	30.8 (1)	5.0 (7)	29.0 (6)	27.8 (4)	4.1 (5)	21.7 (4)	19.2 (8)
Nb	27.6 (7)	21.7 (2)	5.9 (7)	28.4 (6)	20.3 (6)	5.1 (1)	22.0 (5)	20.1 (7)
Cr	13.8 (5)	17.2 (9)	0.7 (4)	23.2 (8)	27.0 (8)	1.7 (9)	33.4 (3)	35.2 (4)

Figure 5.18 shows the XRD diffraction patterns of the as-cast alloys. The patterns of alloys containing 15, 25, and 35 at.% Cr were indexed with a main BCC phase. Small peaks of second phases were also observed. These peaks can be fitted to a FCC structure (Cu-type, Fm-3m). However, for the $(TiVNb)_{65}Cr_{35}$ alloy, the FCC peaks are very small, indicating a small fraction of that phase. As shown in Table 5.12, increasing the Cr amount decreases the BCC lattice parameter. This is probably due to the smaller atomic radius of Cr compared to the other elements (See Appendix II).

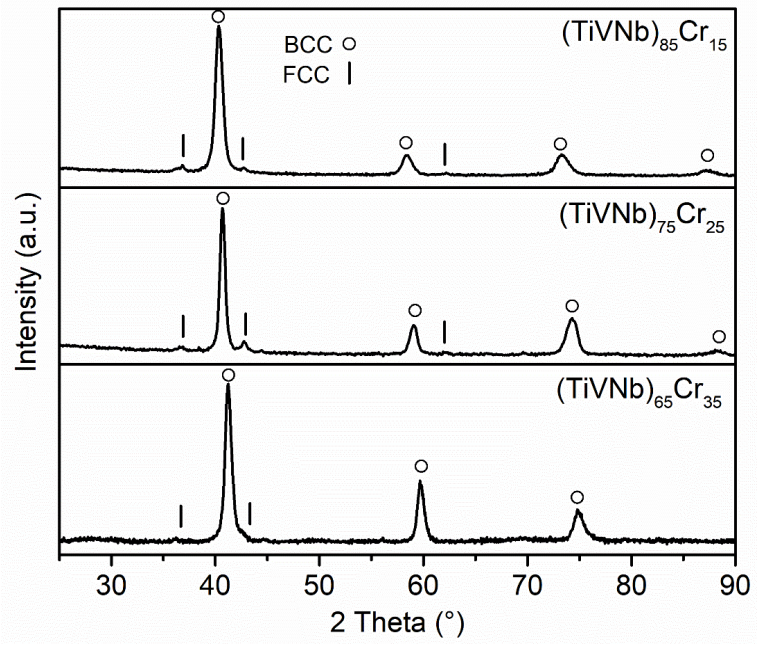

Figure 5.18 – Indexed XRD patterns for samples in as cast condition. Alloy's compositions are indicated on the figure.

Table 5.12 – BCC lattice parameters in the as-cast condition for alloys with different Cr content. The error in the last significant digit is indicated in parenthesis.

Alloy	Lattice parameter (Å)
$(TiVNb)_{85}Cr_{15}$	3.158(1)
$(TiVNb)_{75}Cr_{25}$	3.122(1)
$(TiVNb)_{65}Cr_{35}$	3.105(6)

The XRD results agree with the micrographs that reveals a multiphase microstructure. The BCC phase was associated with the bright and dark gray regions seen in Figure 5.17. From Table 5.11 these two regions have close chemical compositions, indicating that the BCC phase is a solid solution with a range of composition. The minor FCC phase was associated with the black Ti-rich precipitates. This affirmation was supported by EBSD analysis of the $(TiVNb)_{75}Cr_{25}$ alloy. As shown in Figure 5.19, while the matrix is the BCC phase, the Ti-rich precipitates are the FCC phase.

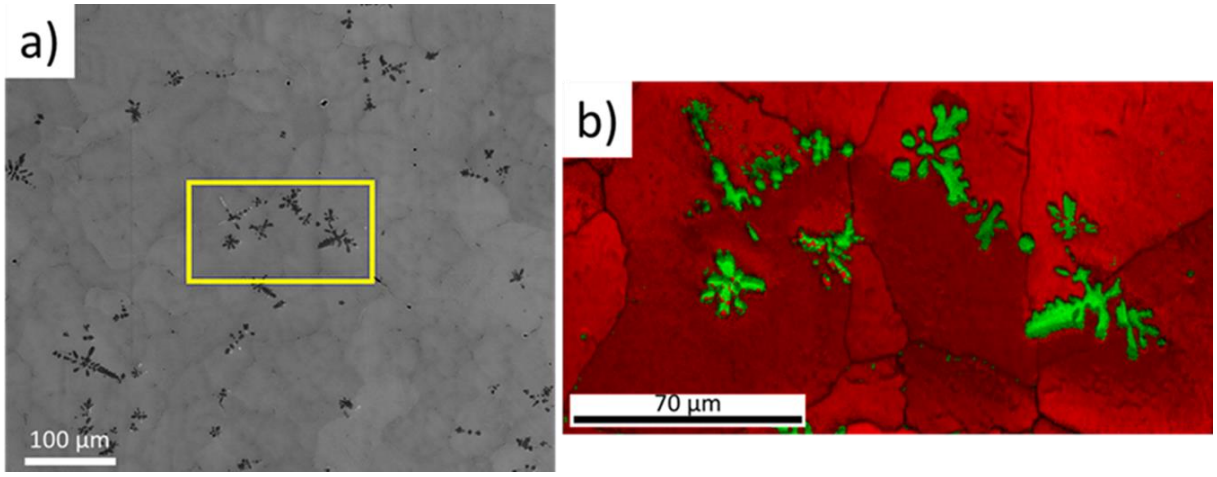

Figure 5.19 – FCC Ti-rich precipitates embedded in the BCC matrix in $(TiVNb)_{75}Cr_{25}$ multi-principal element alloy. (a) Secondary electrons SEM image. The yellow rectangle indicates the EBSD acquisition area. (b) EBSD phase map. The red and green areas were indexed respectively as BCC and FCC phase structures.

The presence of the FCC Ti-rich phase was surprising. To the best of our knowledge, the FCC Ti-rich phase's appearance has never been reported in the Ti-V-Nb-Cr system. Also, FCC-structured Ti was only experimentally identified under particular

conditions, i.e., specifical heat-treatments or several plastic deformations [58–60]. Titanium is allotropic and exhibits a hexagonally close-packed structure at ambient conditions (α-Ti). At high temperatures, the stable phase is a body-centered cubic structure, the β phase. Another allotropic Ti such as the α', ω and the martensite α'' can be found in Ti alloys' literature [61]. However, none of these phases could be indexed to the second phase peaks. Recently, the allotropic FCC-Ti was reported in the $Ti_{37}Nb_{28}Mo_2C_7$ alloy [62]. The FCC-Ti was experimentally observed and ab-initio calculations revelated that the lattice structure results from a rearrangement induced by interstitial carbon atoms. However, there is no evidence of contamination by interstitial atoms. Thus, a better understanding of this precipitation phenomenon demands further investigation, which is out of this study's scope.

5.3.3 Hydrogen storage of the $(TiVNb)_{100-x}Cr_x$ alloys

Fig. 5.20 shows the kinetic measurements of the first hydrogen absorption for the $(TiVNb)_{100-x}Cr_x$ alloys in the as-cast condition. Even under mild conditions, i.e., room temperature and 2000 kPa of H_2, the alloys immediately absorb hydrogen at a fast rate without any prior activation treatment, achieving a hydrogen-to-metal ratio of approximately 2.

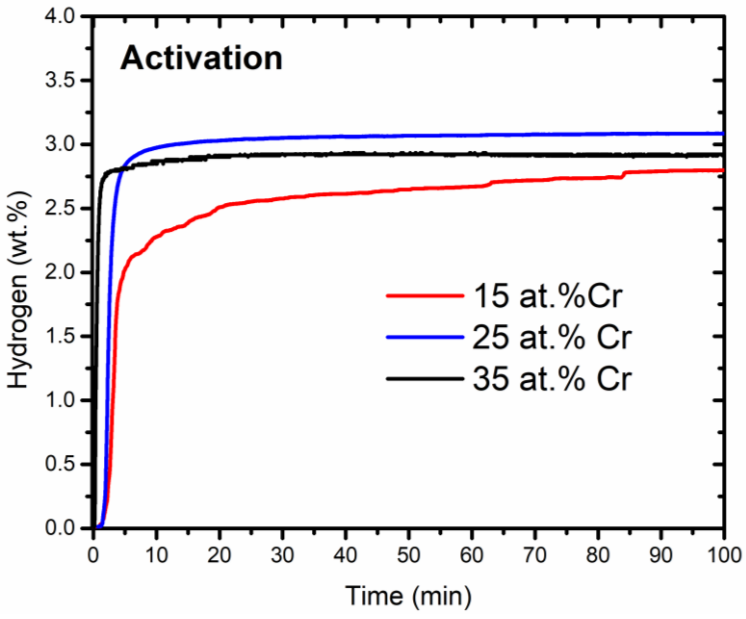

Figure 5.20 – Kinetic curves of the first hydrogen absorption of the $(TiVNb)_{100-x}Cr_x$ alloys. Experiments performed at 24°C and under 2000kPa of hydrogen.

The absence of a long incubation time and the fast hydrogen absorption kinetics at room temperature with no activation procedure need is very important for practical applications. Usually, the practical applications of metal hydrides are limited due to its sluggish first hydrogenation due to the presence of stable and dense surface oxides and hydroxides. In this step is desired an easy activation process to minimize container pressure and temperature requirements for the one-time activation [63].

Figure 5.21 shows the XRD patterns after the first hydrogenation of the three studied alloys. The XRD analysis of the $(TiVNb)_{85}Cr_{15}$ and $(TiVNb)_{75}Cr_{25}$ reveals structural changes due to the hydrogen uptake. As shown in figure 5.21, the XRD patterns of the alloys containing 15 and 25 at.% Cr after activation were indexed as a mixture of phases containing a main FCC phase with small FCC peaks related to the Ti-rich precipitates. The major FCC phase was associated with the dihydride phase (CaF_2-type structure), typically resulting from full hydrogenation of BCC alloys [64,65]. A broadband was also observed around 40° that seems related to some BCC fraction that was not transformed into FCC. Nevertheless, these results agree with the kinetics analysis (Figure 5.20) and confirmed that the $(TiVNb)_{85}Cr_{15}$ and $(TiVNb)_{75}Cr_{25}$ alloys absorb a significant amount of hydrogen at room temperature, reaching a hydrogen uptake close H/M = 2.

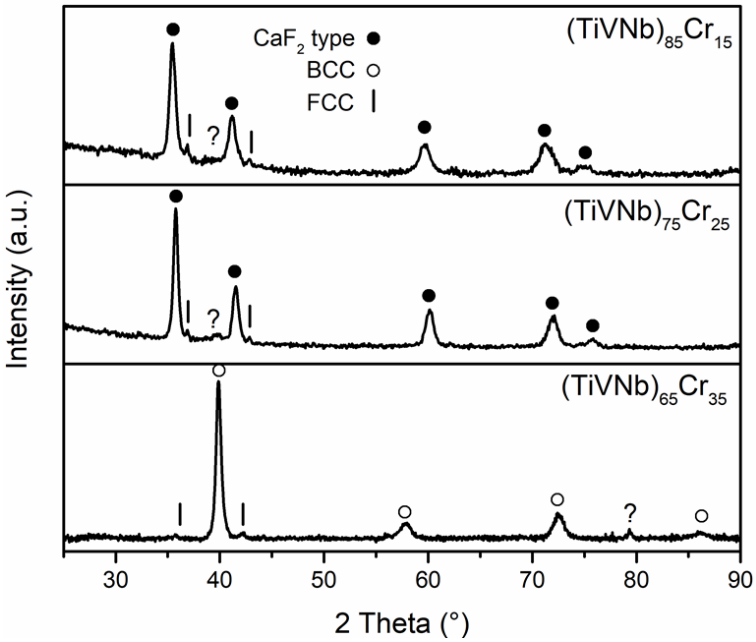

Figure 5.21 – Indexed XRD patterns of $(TiVNb)_{85}Cr_{15}$, $(TiVNb)_{75}Cr_{25}$ and $(TiVNb)_{65}Cr_{35}$ alloys after the first hydrogen absorption.

The XRD pattern of the $(TiVNb)_{65}Cr_{35}$ alloy also shows a mixture of phases. However, the main phase is BCC and no FCC phase was found. Comparing with the as-cast condition, only a slight increase of the BCC lattice parameter was observed from 3.105(1) Å up to 3.188(1) Å. The increase of unit cell is related to the hydrogen accommodation on the interstitial sites of the BCC phase and, according to the Peisl relationship, in metal hydrides, the unit cell volume varies from 2 to 2.9 $Å^3$ per hydrogen atom in the host lattice. Therefore, 2.46 A^3, resulting in hydrogen to metal ratio of about 0.42 to 0.62. The measured capacity by Sievert's technique (H/M~2) is significantly higher than the calculated from XRD data. Perhaps the explanation lies in the fact that it was used as a post-mortem sample to acquire the XRD data. In this case, there is a possibility of hydrogen desorption in the meantime between the volumetric analysis and the XRD acquisition. Thus, to confirm our hypothesis and verify the equilibrium conditions, the acquisitions of room temperature absorption/desorption PCIs were performed.

Fig. 5.22 shows the PCI of the investigated alloys at 24°C and up to 2000 kPa. Before the PCI measurements, a heat treatment at 450°C under dynamic vacuum for 2h was performed. The absorption/desorption plateau pressures under thermodynamic equilibrium conditions and reversible hydrogen storage capacities could be assessed

from the PCI curves. As seen, the $(TiVNb)_{85}Cr_{15}$ alloy achieved a hydrogen-to-metal ratio close to 1.9, which corresponds to a gravimetric capacity of about 2.99 wt.%. The PCI curve exhibits low absorption equilibrium pressure (~1 kPa), while the desorption pressure was too low to be measured. The low desorption plateau pressure hinders the hydrogen release for desorption, resulting in a low reversible hydrogen storage capacity at room temperature. The PCI curve of the $(TiVNb)_{75}Cr_{25}$ alloy displayed two absorption plateaus, reaching a hydrogen uptake of about H/M = 1.8, which corresponds to a gravimetric capacity of 2.85 wt.%. Again, the desorption pressure was too low to be measured, also indicating a low reversible capacity. From figure 5.22, one can see that the $TiVNb_{65}Cr_{35}$ alloy achieved a H/M = 1.79, which corresponds to a gravimetric capacity of about 2.9 wt.% from the first hydrogenation cycle. Additionally, this alloy achieved larger reversible hydrogen storage capacities than the alloys containing 15 and 25 at.% Cr, where its partial dehydrogenation, corresponds to an approximatively 1.5 wt.% (H/M = 1). The reason is the increase of plateau pressure. The sample can absorb and partially desorb hydrogen at room temperature because the desorption plateau pressure at room temperature is between 10 and 20 kPa.

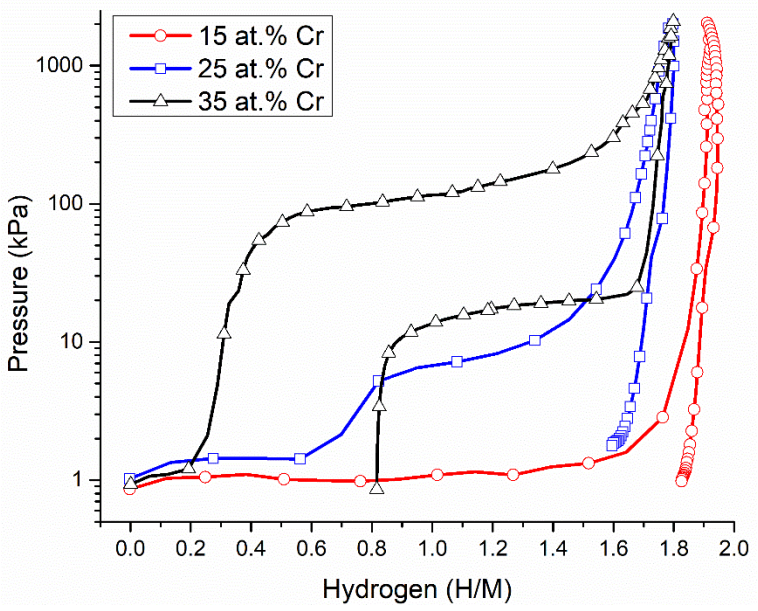

Figure 5.22 – PCI absorption/desorption isotherms carried out at 24 °C. The compositions are indicated in the figure.

As shown in Figure 5.22, the $(TiVNb)_{65}Cr_{35}$ alloy retains a partial fraction of its absorbed hydrogen. Probably, this behavior occurs due to the low plateau pressure of the monohydride. To verify the amount of hydrogen retained in the crystal lattice, a XRD analysis of the $(TiVNb)_{65}Cr_{35}$ alloy after the PCI cycle was performed, and the data is displayed in Figure 5.23. As can be seen, the alloy is composed of a Ti-FCC precipitate and a BCC structure with a lattice parameter of a = 3.188(2) Å. This lattice parameter indicates a volume expansion from the as-cast condition (~2.46 A^3), resulting in hydrogen to metal ratio of about 0.42 to 0.62., which corroborates with the remaining hydrogen measured by the volumetric technique $(TiVNb)_{65}Cr_{35}$ alloy. Additionally, the BCC lattice parameter is the same after the kinetics measurements (Fig 5.21). This could be explained by the relatively high desorption plateau pressure (10 and 20 kPa). As the sample had to be removed from the sample holder after kinetics, the vacuum and the air exposition induce the partial dehydrogenation, confirming the initial hypothesis.

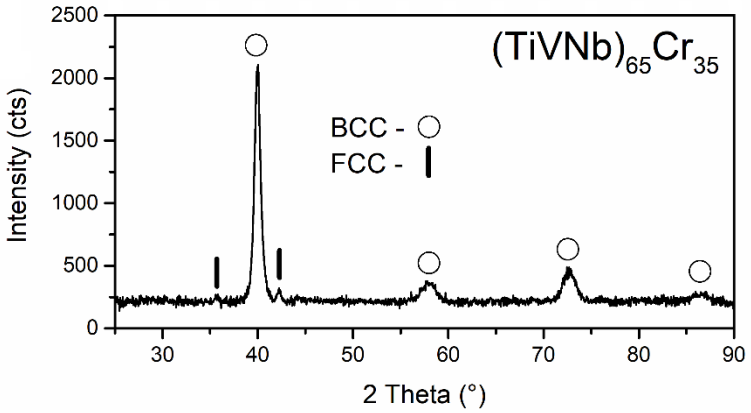

Figure 5.23 – XRD patterns of $(TiVNb)_{65}Cr_{35}$ alloy after the PCI cycle.

The extensive pursuit of metal hydrides that can operate at mild conditions is a central key for metal hydrides' practical applications. Usually, refractory body-centered cubic HEAs can absorb hydrogen at room temperature, but their desorption reaction needs high temperatures [20,39]. As shown in Figure 5.22, the amount of Cr in the BCC lattice of the Ti-V-Nb-Cr system has changed the system's thermodynamics, where the plateau pressure was increased by increasing the Cr amount. This effect was more pronounced in the $(TiVNb)_{65}Cr_{35}$ alloy, which can absorb and desorb hydrogen at room temperature due to its relatively high dihydride plateau pressure.

The thermodynamics changing explanation lies in increasing the number of inert elements (Cr) around the interstitial sites, where the hydrogen atoms are accommodated, reducing the strong hydrogen binding energy and allowing reversible hydrogenation/dehydrogenation reactions at room temperature [66]. Thus, this work successfully proposed destabilizing a HEA base metal hydride by adding a non-hydride element. This was the first BCC-HEA metal hydride that can operate at room temperature to the best of our knowledge.

6 GENERAL DISCUSSION

The generated data set was thoroughly analyzed, allowing the understanding and correlation between structure, property, and processing in each case. This understanding was correlated with the design strategy, and a brief overview with a general discussion is given below.

At first, the HEBM process was employed to synthesize the new lightweight alloys of the Mg-V-Al-Cr-Ni system for hydrogen storage applications. The study of ternaries MgVAl, MgVCr, MgVNi, quaternaries MgVAlCr, MgVAlNi, MgVCrNi, and quinary MgVAlCrNi alloys suggests that a single-phase solid solution for the Mg-V-A-Cr-Ni system can be only obtained when the configurational entropy is maximized, i.e., for the equiatomic MgVAlCrNi alloy. The lightweight MgVAlCrNi HEA with a single BCC structure can be produced by HEBM both under 3.0 MPa of hydrogen and 0.7 MPa of argon. The two processing conditions resulted in powders composed of a single-phase BCC solid solution with similar morphology. The hydrogen storage capacity of the MgVAlCrNi HEA is low (~0.3 wt.%), and no high entropy hydride is formed when the sample is produced by HEBM under hydrogen pressure.

Aiming to increasing the alloys' hydrogen affinity, the off-stoichiometric $Mg_{28}V_{28}Al_{19}Cr_{19}Ni_6$ and $Mg_{26}V_{31}Al_{31}Cr_6Ni_6$ HEAs were synthesized by HEBM under hydrogen pressure. Both alloys presented a mixture of BCC solid solution and secondary phases such as MgH_2 with low hydrogen storage capacity. The low hydrogen affinity of the studied HEAs is associated with the enthalpy of hydrogen solution ($\overline{\Delta H_\infty}$) of the alloying elements, which are positive for most of the elements of the Mg-V-Al-Cr-Ni system. Only V has negative enthalpy of solution. Even increasing the amount of Mg and V in the non-equiatomic alloys, the hydrogen storage capacity is not improved because Mg (although is a strong hydride former element) also has a positive enthalpy of solution of hydrogen. The study of the Mg-V-Al-Cr-Ni HEAs system shows for the first time that the mean enthalpy of hydrogen solution is an important parameter to be considered for designing lightweight Mg-containing HEAs for hydrogen storage applications.

It is worth mentioning that the empirical approach used in the study of the Mg-V-Al-Cr-Ni system demands several experiments. To overcome this problem and improve

the alloys' hydrogen affinity, a semiempirical approach to design single-phase BCC HEAs for hydrogen storage was proposed. It was selected the Mg-Al-Ti-Mn-Nb system, with a higher fraction of hydride forming elements. Four parameters were considered for alloying design: the single parameter φ proposed by Y. Ye et al. [12] was employed to select a composition with a high tendency to form a single-phase solid solution; calculation of VEC was used to indicate the tendency to form a BCC solid solution; finally, the alloys' affinity with hydrogen was assessed trough the values of $\overline{\Delta H_{\infty}}$ and $\overline{\Delta H_f^o}$. The method was successfully applied to screen compositions of interest in the studied system and the $Mg_{12}Al_{11}Ti_{33}Mn_{11}Nb_{33}$ alloy was selected among 1326 calculated compositions.

The designed $Mg_{12}Al_{11}Ti_{33}Mn_{11}Nb_{33}$ alloy was produced by HEBM under argon atmosphere. Its structural characterization reveals that we succeed in producing a homogenous single BCC alloy. The hydrogen absorption measurements of the BCC alloy $Mg_{12}Al_{11}Ti_{33}Mn_{11}Nb_{33}$ synthesized under the argon atmosphere forming a monohydride (BCC) with a gravimetric storage capacity of 1.75 wt.%, which was released after DSC analysis. A face-centered cubic hydride (CaF_2-type) was produced directly by reactive milling under hydrogen pressure, which undergoes a phase transformation to a BCC structure after hydrogen desorption, releasing approximately 1.75 wt.% of hydrogen. The coincident-released hydrogen capacity for the BCC absorbed and the FCC synthesized by RM calls attention. This phenomenon still unclear, and further investigation is needed.

The hydrogenation/dehydrogenation performance of the $Mg_{12}Al_{11}Ti_{33}Mn_{11}Nb_{33}$ alloy deserves attention. Usually, refractory BCC HEA metal hydrides absorb hydrogen at room temperature, achieving a hydrogen uptake of about H/M = 2. When produced by reactive milling, these alloys also exhibit a high tendency to form dihydrides with FCC structure [43]. Due to their very low plateau pressure, the desorption is associated with very high temperatures. For the $Mg_{12}Al_{11}Ti_{33}Mn_{11}Nb_{33}$ alloy, a hydrogen uptake H/M = 2 was not found. At first, this could indicate a kinetic obstacle. However, even when produced by reactive high energy ball milling, a severe condition, the sample's capacity is the same. Also, the H-sorption demands high temperatures. This performance was similar to that reported for other Mg-containing BCC HEA metal hydrides [45,46], indicating that the Mg's intrinsic features severely affect the hydrogen storage performance. Despite that, our findings pointing out that the semiempirical design

approach presented here can indeed be used as a convenient way to design alloys for hydrogen storage and can be applied to screen different systems in HEAs' endless compositional space. By comparing with approach presented in session 5.1, when it was studied the Mg-V-Al-Cr-Ni system, many experiments have been saved, and it was obtained a HEA with enhanced hydrogen storage properties.

Finally, a critical assessment of the influence of non-hydride forming elements in a ternary system of hydride forming elements (TiVNb) was carried out. The design strategy adopted on this part of the work differs from the previous one. Firstly, the effect of adding non-hydride forming elements in the TiVNb system was investigated using the CALPHAD method. Thus, the thermodynamic phase stability of the TiVNbM (M = Cr, Mn, Fe, Co and Ni) was investigated, and Cr was selected due to the high tendency to stabilize BCC solid solution. Therefore, the $(TiVNb)_{100-x}Cr_x$ alloys (with x = 15, 25 and 35 at.% Cr) were produced. The structural characterization reveals that the three alloys were composed of major BCC phase, which agrees with the thermodynamic calculations and reveals a successful design. In a second moment, the hydrogen storage properties were evaluated. The alloys absorb hydrogen at room temperature without any activation treatment, achieving a hydrogen uptake about H/M = 2. The PCI measurements have shown that increasing the Cr amount increases the equilibrium pressures. As shown, tunable H storage properties can be achieved by controlling the alloy's Cr content in a range between 15 to 35 at.%. It was found that the $(TiVNb)_{65}Cr_{35}$ exhibits an outstanding combination of properties once its reversible hydrogen storage capacity is 1.65 wt.% H is comparable to $TiFeH_2$, but the activation of the $(TiVNb)_{65}Cr_{35}$ alloy is relatively easy, a feature that restricts the TiFe large-scale application.

The findings from the Ti-V-Nb-Cr system study indicate that the strategy to select alloys composition is very appropriate. The approach consists of destabilizing a well-known system by adding or controlling non-hydride forming elements. Of course, this approach can be useful to screening compositions in several alloy systems inside the vast HEA’s compositional field. However, the described design approach cannot be applied in the Mg-V-Al-Cr-Ni and Mg-Al-Ti-Mn-Nb systems due to the absence of CALPHAD databases combining transition metals and alkaline/alkaline earth elements, making the empirical and semiempirical approach very useful and important.

It was demonstrated that HEAs' design for hydrogen storage applications can be very suitable for reducing the number of experiments and tailoring the HEAs hydrogen storage properties. Despite that, adjustments on the guideline parameters can be incorporated to obtain alloys with different features, e.g., to design multicomponent intermetallic based metal hydrides, with Laves phase structure. As a recent research area, HEA based metal hydrides demands constant updating. There are several topics of studies that deserve attention and should be elucidated. For instance, the role of Mg when combined with transition metal alloying elements. Undoubtedly, further new findings will greatly enrich the research area and should be incorporated into the design strategies discussed in this thesis. Nevertheless, this thesis brought to light a starting point to advance HEAs' technological feasibility with optimized and controlled hydrogen storage properties.

7 CONCLUSIONS

The study of the high entropy alloys is only at the beginning and holds promise of interesting findings. In this way, our results can contribute in many aspects to pave the way towards the design of suitable HEAs for hydrogen applications.

Initially, the Mg-V-Al-Cr-Ni system was studied. The goal of this step was to obtain single-phase BCC lightweight alloys with attractive hydrogen properties. The element selection was mainly based on their ability to form or not metal hydrides. However, Mg and Al were firstly chosen because they are lightweight elements. The main conclusions of this study were:

- The MgVAlCrNi single-phase BCC-HEA with a density of 5.48 g/cm^3 was synthesized by reactive milling.
- The MgVAlCrNi alloy exhibited poor hydrogen storage properties, achieving a $H/M \approx 0.3$. This behavior was associated with the alloy's low hydrogen affinity. Thus, it was suggested that the key to producing suitable HEAs for hydrogen storage applications is controlling the mean enthalpy of hydrogen solution ($\overline{\Delta H_\infty}$) of the alloying elements.

The second step of this work aimed to obtain an Mg-containing single-phase BCC-HEA with improved hydrogen properties, minimizing the number of experiments. In this step, the following conclusions were drawn:

- A semi-empirical approach was successfully applied to screening compositions inside the Mg-Al-T-Mn-Nb system. Looking for intersections between pre-set semiempirical parameters ($\varphi, VEC, \overline{\Delta H_\infty}$ and $\overline{\Delta H_f^o}$), the $Mg_{13}Al_{11}Ti_{33}Mn_{11}Nb_{33}$ alloy was proposed. This alloy presents a single-phase BCC when synthesized by high energy ball milling under Ar atmosphere.
- The maximum hydrogen uptake presented for the $Mg_{13}Al_{11}Ti_{33}Mn_{11}Nb_{33}$ alloy was about $H/M = 1$, differing from the typical behavior of refractory BCC alloys, which usually achieve a $H/M \approx 2$. Even with this lower hydrogen uptake, the gravimetric capacity of the $Mg_{12}Al_{11}Ti_{33}Mn_{11}Nb_{33}$ alloy (1.75 wt.%) is still competitive with other

refractory HEAs. This is a very remarkable feature since the gravimetric capacity has practical technological importance.

- From a theoretical perspective, this study highlighted the strong Mg's influence in BCC-HEAs. Although Mg is a strong hydride former element, its enthalpy of hydrogen solution is very positive. Therefore, this parameter should be considered in the designing approach. Also, the operation conditions of Mg-containing HEAs are very different from refractory single-phase BCC-HEAs, which deserve further investigation.

The study of the Ti-V-Nb-Cr system aimed to investigate the effects of adding a non-hydride-forming alloying element in a system composed of hydride-forming elements. In this third step, the following conclusions could be drawn:

- Via CALPHAD approach, the thermodynamic phase stability of the TiVNbM (M = Cr, Mn, Fe, Co and Ni) alloys was investigated. Cr was selected as the fourth alloying element since the CALPHAD predictions indicate a higher tendency to form single-phase BCC solid solutions. Therefore, the $(TiVNb)_{100-x}Cr_x$ alloys (x = 15, 25 and 35 at.%) were prepared by arc-melting, and both samples crystallize as a major single-phase BCC structure.
- Via acquisition of PCT isotherms it was found that the equilibrium plateau pressure of the BCC alloys increases by increasing the Cr/(TiVNb) ratio. Additionally, the hydrogen uptake ($H/M \sim 2$) is the same for the three compositions, indicating no substantial loss of maximum capacity. Therefore, it was demonstrated the feasibility of obtaining HEAs with attractive and tunable hydrogen storage properties by adding and controlling the amount of a non-hydride forming element (Cr) in a system composed of hydride forming elements.
- The $(TiVNb)_{85}Cr_{15}$, $(TiVNb)_{75}Cr_{25}$, and $(TiVNb)_{65}Cr_{35}$ alloys presented rapid first hydrogenation without prior heat treatment, which has technological implications since the hydrogen storage tank could be directly filled with the as-cast alloy.

8 SUGGESTION FOR FUTURE WORKS

- Considering that the influence of Mg in BCC-HEAs is still an open question, affecting the operational conditions and the H absorption and desorption thermodynamics properties, it is suggested to apply first-principles methods to investigate Mg-containing BCC HEA-based metal hydrides.

- Taking into account the knowledge concerning the Ti-V-Nb-Cr system, the study of incorporating Mg in the Ti-V-Nb-Cr system should be conducted to understand Mg's role in the hydrogen storage properties of multicomponent alloys.

- As it was shown, the alloys of Ti-V-Nb-Cr system promptly absorb hydrogen without any activation procedure. To better understand this behavior, it is suggested the study of the presence of surface oxides and hydroxides that can prevent the first hydrogenation. Therefore, a dedicated experiment to measure the oxygen content phases as a function of time should be conducted.

9 REFERENCES

[1] T.Y. Wei, K.L. Lim, Y.S. Tseng, S.L.I. Chan, A review on the characterization of hydrogen in hydrogen storage materials, Renew. Sustain. Energy Rev. 79 (2017) 1122–1133. doi:10.1016/j.rser.2017.05.132.

[2] J. Bellosta von Colbe, J.R. Ares, J. Barale, M. Baricco, C. Buckley, G. Capurso, N. Gallandat, D.M. Grant, M.N. Guzik, I. Jacob, E.H. Jensen, T. Jensen, J. Jepsen, T. Klassen, M. V. Lototskyy, K. Manickam, A. Montone, J. Puszkiel, S. Sartori, D.A. Sheppard, A. Stuart, G. Walker, C.J. Webb, H. Yang, V. Yartys, A. Züttel, M. Dornheim, Application of hydrides in hydrogen storage and compression: Achievements, outlook and perspectives, Int. J. Hydrogen Energy. 44 (2019) 7780–7808. doi:10.1016/j.ijhydene.2019.01.104.

[3] M. V Lototskyy, V.A. Yartys, B.G. Pollet, R.C.B. Bowman Jr, Metal hydride hydrogen compressors : A review, Int. J. Hydrogen Energy. 39 (2014) 5818–5851. doi:10.1016/j.ijhydene.2014.01.158.

[4] J. Huot, Metal Hydrides, in: M. Hirscher (Ed.), Handb. Hydrog. Storage New Mater. Futur. Energy Storage, Wiley-VCH Verlag GmbH & Co. KGaA, 2010: pp. 81–116. doi:10.1002/9783527629800.

[5] B. Cantor, I.T.H. Chang, P. Knight, A.J.B. Vincent, Microstructural development in equiatomic multicomponent alloys, Mater. Sci. Eng. A. 375–377 (2004) 213–218. doi:10.1016/j.msea.2003.10.257.

[6] J.W. Yeh, S.K. Chen, S.J. Lin, J.Y. Gan, T.S. Chin, T.T. Shun, C.H. Tsau, S.Y. Chang, Nanostructured high-entropy alloys with multiple principal elements: Novel alloy design concepts and outcomes, Adv. Eng. Mater. 6 (2004) 299–303. doi:10.1002/adem.200300567.

[7] Y.F. Ye, Q. Wang, J. Lu, C.T. Liu, Y. Yang, High-entropy alloy: challenges and prospects, Mater. Today. 19 (2016) 349–362. doi:10.1016/j.mattod.2015.11.026.

[8] X. Yang, Y. Zhang, Prediction of high-entropy stabilized solid-solution in multi-component alloys, Mater. Chem. Phys. 132 (2012) 233–238. doi:10.1016/j.matchemphys.2011.11.021.

[9] S. Guo, C. Ng, J. Lu, C.T. Liu, Effect of valence electron concentration on stability

of fcc or bcc phase in high entropy alloys, J. Appl. Phys. 109 (2011). doi:10.1063/1.3587228.

[10] S. Guo, C.T. Liu, Phase stability in high entropy alloys: Formation of solid-solution phase or amorphous phase, Prog. Nat. Sci. Mater. Int. 21 (2011) 433–446. doi:10.1016/S1002-0071(12)60080-X.

[11] Y.F. Ye, Q. Wang, J. Lu, C.T. Liu, Y. Yang, The generalized thermodynamic rule for phase selection in multicomponent alloys, Intermetallics. 59 (2015) 75–80. doi:10.1016/j.intermet.2014.12.011.

[12] Y.F. Ye, Q. Wang, J. Lu, C.T. Liu, Y. Yang, Design of high entropy alloys: A single-parameter thermodynamic rule, Scr. Mater. 104 (2015) 53–55. doi:10.1016/j.scriptamat.2015.03.023.

[13] P. Edalati, R. Floriano, A. Mohammadi, Y. Li, G. Zepon, H.W. Li, K. Edalati, Reversible room temperature hydrogen storage in high-entropy alloy TiZrCrMnFeNi, Scr. Mater. 178 (2020) 387–390. doi:10.1016/j.scriptamat.2019.12.009.

[14] J. Sarac, Baran; Zadorozhnyy, Vladislav; Berdonosova, Elena; Ivanov, Yurii; Klyamkin, Semen; Gumrukcu, Selin; Sarac, A.Sezai; Korol, Artem; Semenov, Dmitry; Zadorozhnyy, Mikhail; Sharma, Adit; Greer, A; Eckert, Hydrogen storage performance of the multi-principal-component CoFeMnTiVZr alloy in electrochemical and gas-solid reactions, (2020) 24613–24623. doi:10.1039/d0ra04089d.

[15] V., B. Sarac, E. Berdonosova, T. Karazehir, A. Lassnig, C. Gammer, M. Zadorozhnyy, S. Ketov, S. Klyamkin, J. Eckert, Evaluation of hydrogen storage performance of ZrTiVNiCrFe in electrochemical and gas-solid reactions, Int. J. Hydrogen Energy. 45 (2020) 5347–5355. doi:10.1016/j.ijhydene.2019.06.157.

[16] C. Zlotea, M.A. Sow, G. Ek, J.P. Couzinié, L. Perrière, I. Guillot, J. Bourgon, K.T. Møller, T.R. Jensen, E. Akiba, M. Sahlberg, Hydrogen sorption in TiZrNbHfTa high entropy alloy, J. Alloys Compd. 775 (2019) 667–674. doi:10.1016/j.jallcom.2018.10.108.

[17] T.W. Na, K.B. Park, S.Y. Lee, S.M. Yang, J.W. Kang, T.W. Lee, J.M. Park, K. Park, H.K. Park, Preparation of spherical TaNbHfZrTi high-entropy alloy powders by a

hydrogenation–dehydrogenation reaction and thermal plasma treatment, J. Alloys Compd. 817 (2020) 152757. doi:10.1016/j.jallcom.2019.152757.

[18] D. Karlsson, G. Ek, J. Cedervall, C. Zlotea, K.T. Møller, T.C. Hansen, J. Bednarčík, M. Paskevicius, M.H. Sørby, T.R. Jensen, U. Jansson, M. Sahlberg, Structure and Hydrogenation Properties of a HfNbTiVZr High-Entropy Alloy, Inorg. Chem. 57 (2018) 2103–2110. doi:10.1021/acs.inorgchem.7b03004.

[19] M. Sahlberg, D. Karlsson, C. Zlotea, U. Jansson, Superior hydrogen storage in high entropy alloys, Sci. Rep. 6 (2016) 36770. doi:10.1038/srep36770.

[20] J. Montero, G. Ek, L. Laversenne, V. Nassif, G. Zepon, M. Sahlberg, C. Zlotea, Hydrogen storage properties of the refractory Ti–V–Zr–Nb–Ta multi-principal element alloy, J. Alloys Compd. 835 (2020) 155376. doi:10.1016/j.jallcom.2020.155376.

[21] J.W. Yeh, Physical Metallurgy of High-Entropy Alloys, Jom. 67 (2015) 2254–2261. doi:10.1007/s11837-015-1583-5.

[22] R.A. Swalin, Thermodynamics of Solids, Second Ed., John Wiley & Sons, New York, 1972.

[23] E.J. Pickering, N.G. Jones, High-entropy alloys: a critical assessment of their founding principles and future prospects, Int. Mater. Rev. 61 (2016) 183–202. doi:10.1080/09506608.2016.1180020.

[24] P.J. Spencer, A brief history of CALPHAD, Comput. Coupling Phase Diagrams Thermochem. 32 (2008) 1–8. doi:10.1016/j.calphad.2007.10.001.

[25] O. Redlich, A.T. Kister, Algebraic representation of thermodynamic properties and the classification, Ind. Eng. Chem. 40 (1948) 345–348. doi:10.1021/ie50458a036.

[26] D.J.M. King, S.C. Middleburgh, A.G. Mcgregor, M.B. Cortie, Predicting the formation and stability of single phase high-entropy alloys, Acta Mater. 104 (2016) 172–179. doi:10.1016/j.actamat.2015.11.040.

[27] Y. Zhang, Y.J. Zhou, J.P. Lin, G.L. Chen, P.K. Liaw, Solid-solution phase formation rules for multi-component alloys, Adv. Eng. Mater. 10 (2008) 534–538. doi:10.1002/adem.200700240.

[28] A. Takeuchi, K. Amiya, T. Wada, K. Yubuta, W. Zhang, A. Makino, Entropies in alloy design for high-entropy and bulk glassy alloys, Entropy. 15 (2013) 3810–3821.

doi:10.3390/e15093810.

[29] A. Takeuchi, A. Inoue, Classification of Bulk Metallic Glasses by Atomic Size Difference, Heat of Mixing and Period of Constituent Elements and Its Application to Characterization of the Main Alloying Element, Mater. Trans. 46 (2005) 2817–2829. doi:10.2320/matertrans.46.2817.

[30] G.A. Mansoori, N.F. Carnahan, K.E. Starling, T.W. Leland, Equilibrium Thermodynamic Properties of the Mixture of Hard Spheres, J. Chem. Phys. 54 (1971) 1523–1525. doi:10.1063/1.1675048.

[31] M. Dornheim, Thermodynamics of Metal Hydrides: Tailoring Reaction Enthalpies of Hydrogen Storage Materials, in: Thermodyn. - Interact. Stud. - Solids, Liq. Gases, 2011. doi:10.5772/21662.

[32] D.B. Miracle, O.N. Senkov, A critical review of high entropy alloys and related concepts, Acta Mater. 122 (2017) 448–511. doi:10.1016/j.actamat.2016.08.081.

[33] M.C. Gao, D.B. Miracle, D. Maurice, X. Yan, Y. Zhang, J.A. Hawk, High-entropy functional materials, J. Mater. Res. 33 (2018) 3138–3155. doi:10.1557/jmr.2018.323.

[34] F. Stein, M. Palm, G. Sauthoff, Structure and stability of Laves phases. Part I. Critical assessment of factors controlling Laves phase stability, Intermetallics. 12 (2004) 713–720. doi:10.1016/j.intermet.2004.02.010.

[35] Y.-F. Kao, S.-K. Chen, J.-H. Sheu, J.-T. Lin, W.-E. Lin, J.-W. Yeh, S.-J. Lin, T.-H. Liou, C.-W. Wang, Hydrogen storage properties of multi-principal-component CoFeMnTixVyZrz alloys, Int. J. Hydrogen Energy. 35 (2010) 9046–9059. doi:10.1016/j.ijhydene.2010.06.012.

[36] I. Kunce, M. Polanski, J. Bystrzycki, Microstructure and hydrogen storage properties of a TiZrNbMoV high entropy alloy synthesized using Laser Engineered Net Shaping (LENS), Int. J. Hydrogen Energy. 39 (2014) 9904–9910. doi:10.1016/j.ijhydene.2014.02.067.

[37] K.H. Young, J. Nei, C. Wan, R. V. Denys, V.A. Yartys, Comparison of C14-and C15-predomiated AB 2 metal hydride alloys for electrochemical applications, Batteries. 3 (2017) 1–19. doi:10.3390/batteries3030022.

[38] M.M. Nygård, G. Ek, D. Karlsson, M. Sahlberg, M.H. Sørby, B.C. Hauback,

Hydrogen storage in high-entropy alloys with varying degree of local lattice strain, Int. J. Hydrogen Energy. 44 (2019) 29140–29149. doi:10.1016/J.IJHYDENE.2019.03.223.

[39] M.M. Nygård, G. Ek, D. Karlsson, M.H. Sørby, M. Sahlberg, B.C. Hauback, Counting electrons - a new approach to tailor the hydrogen sorption properties of high-entropy alloys, Acta Mater. 175 (2019) 121–129. doi:10.1016/j.actamat.2019.06.002.

[40] W. Sun, X. Huang, A.A. Luo, Phase formations in low density high entropy alloys, Calphad Comput. Coupling Phase Diagrams Thermochem. 56 (2017) 19–28. doi:10.1016/j.calphad.2016.11.002.

[41] S. Varalakshmi, M. Kamaraj, B.S. Murty, Formation and stability of equiatomic and nonequiatomic nanocrystalline CuNiCoZnAlTi high-entropy alloys by mechanical alloying, Metall. Mater. Trans. A Phys. Metall. Mater. Sci. 41 (2010) 2703–2709. doi:10.1007/s11661-010-0344-x.

[42] S.K. Dewangan, V.K. Sharma, P. Sahu, V. Kumar, Synthesis and characterization of hydrogenated novel AlCrFeMnNiW high entropy alloy, Int. J. Hydrogen Energy. (2019). doi:10.1016/j.ijhydene.2019.08.113.

[43] J. Montero, C. Zlotea, G. Ek, J. Crivello, L. Laversenne, M. Sahlberg, TiVZrNb Multi-Principal-Element Alloy: Synthesis Optimization, Structural, and Hydrogen Sorption Properties, Molecules. 24 (2019) 2799. doi:10.3390/molecules24152799.

[44] K.M. Youssef, A.J. Zaddach, C. Niu, D.L. Irving, C.C. Koch, A novel low-density, high-hardness, high-entropy alloy with close-packed single-phase nanocrystalline structures, Mater. Res. Lett. 3 (2014) 95–99. doi:10.1080/21663831.2014.985855.

[45] G. Zepon, D.R. Leiva, R.B. Strozi, A. Bedoch, S.J.A. Figueroa, T.T. Ishikawa, W.J. Botta, Hydrogen-induced phase transition of MgZrTiFe0.5Co0.5Ni0.5 high entropy alloy, Int. J. Hydrogen Energy. 43 (2018) 1702–1708. doi:10.1016/j.ijhydene.2017.11.106.

[46] F. Marques, H.C. Pinto, S.J.A. Figueroa, F. Winkelmann, M. Felderhoff, W.J. Botta, G. Zepon, Mg-containing multi-principal element alloys for hydrogen storage: A study of the MgTiNbCr0.5Mn0.5Ni0.5 and Mg0.68TiNbNi0.55 compositions, Int. J. Hydrogen Energy. 45 (2020) 19539–19552. doi:10.1016/j.ijhydene.2020.05.069.

[47] W. Zaïdi, J.P. Bonnet, J. Zhang, F. Cuevas, M. Latroche, S. Couillaud, J.L. Bobet, M.T. Sougrati, J.C. Jumas, L. Aymard, Reactivity of complex hydrides Mg2FeH6, Mg2CoH5 and Mg2NiH4 with lithium ion: Far from equilibrium electrochemically driven conversion reactions, Int. J. Hydrogen Energy. 38 (2013) 4798–4808. doi:10.1016/j.ijhydene.2013.01.157.

[48] L. Lü, M.O. Lai, Mechanical Alloying, First Ed., Springer US, 1998. doi:10.1007/978-1-4615-5509-4.

[49] J. Huot, D.B. Ravnsbæk, J. Zhang, F. Cuevas, M. Latroche, T.R. Jensen, Mechanochemical synthesis of hydrogen storage materials, Prog. Mater. Sci. 58 (2013) 30–75. doi:10.1016/j.pmatsci.2012.07.001.

[50] Y.C. Liao, T.H. Li, P.H. Tsai, J.S.C. Jang, K.C. Hsieh, C.Y. Chen, J.C. Huang, H.J. Wu, Y.C. Lo, C.W. Huang, I.Y. Tsao, Designing novel lightweight, high-strength and high-plasticity Tix(AlCrNb)100-x medium-entropy alloys, Intermetallics. 117 (2020). doi:10.1016/j.intermet.2019.106673.

[51] Y. Qiu, Y.J. Hu, A. Taylor, M.J. Styles, R.K.W. Marceau, A. V. Ceguerra, M.A. Gibson, Z.K. Liu, H.L. Fraser, N. Birbilis, A lightweight single-phase AlTiVCr compositionally complex alloy, Acta Mater. 123 (2017) 115–124. doi:10.1016/j.actamat.2016.10.037.

[52] H. Peisl, Lattice strains due to hydrogen in metals, in: G. Alefeld, J. Völkl (Eds.), Hydrog. Met. I. Top. Appl. Physics. Vol 28, Springer, Berlin, Heidelberg, 1978: pp. 53–74. doi:10.1007/3540087052_42.

[53] R. Griessen, T. Riesterer, Heat of formation models, in: Hydrog. Intermet. Compd. I. Top. Appl. Physics. Vol. 64, Springer, Berlin, Heidelberg, 1988: pp. 219–284. doi:10.1007/3540183337_13.

[54] H. Shen, J. Zhang, J. Hu, J. Zhang, Y. Mao, H. Xiao, X. Zhou, X. Zu, A novel TiZrHfMoNb high-entropy alloy for solar thermal energy storage, Nanomaterials. 9 (2019) 1–9. doi:10.3390/nano9020248.

[55] T. Ungár, Microstructural parameters from X-ray diffraction peak broadening, Scr. Mater. 51 (2004) 777–781. doi:10.1016/j.scriptamat.2004.05.007.

[56] S. Miraglia, D. Fruchart, N. Skryabina, M. Shelyapina, B. Ouladiaf, E.K. Hlil, P. De Rango, J. Charbonnier, Hydrogen-induced structural transformation in TiV0.8Cr1.2

studied by in situ neutron diffraction, J. Alloys Compd. 442 (2007) 49–54. doi:10.1016/j.jallcom.2006.10.168.

[57] M.O. de Marco, Y. Li, H.W. Li, K. Edalati, R. Floriano, Mechanical Synthesis and Hydrogen Storage Characterization of MgVCr and MgVTiCrFe High-Entropy Alloy, Adv. Eng. Mater. 22 (2020) 1–24. doi:10.1002/adem.201901079.

[58] R. Jing, C.Y. Liu, M.Z. Ma, R.P. Liu, Microstructural evolution and formation mechanism of FCC titanium during heat treatment processing, J. Alloys Compd. 552 (2013) 202–207. doi:10.1016/j.jallcom.2012.10.083.

[59] T.N. Prasanthi, C. Sudha, Ravikirana, S. Saroja, Formation and reversion of metastable fcc phase in a Ti-5Ta-2Nb explosive clad, Mater. Charact. 116 (2016) 24–32. doi:10.1016/j.matchar.2016.03.022.

[60] H.C. Wu, A. Kumar, J. Wang, X.F. Bi, C.N. Tomé, Z. Zhang, S.X. Mao, Rolling-induced face centered cubic titanium in hexagonal close packed titanium at room temperature, Sci. Rep. 6 (2016) 1–8. doi:10.1038/srep24370.

[61] C. Li, G. Li, Y. Yang, M. Varlioglu, K. Yang, Martensitic Twinning in Alpha + Beta Ti-3.5Al-4.5Mo Titanium Alloy, J. Metall. 2011 (2011) 1–5. doi:10.1155/2011/924032.

[62] S. Jiang, L. Huang, X. Gao, G. Liu, R. Zhang, Y. Jiao, S. Peng, Q. An, S. Wang, L. Geng, Interstitial carbon induced FCC-Ti exhibiting ultrahigh strength in a Ti37Nb28Mo28-C7 complex concentrated alloy, Acta Mater. 203 (2021). doi:10.1016/j.actamat.2020.10.075.

[63] G. Sandrock, Panoramic overview of hydrogen storage alloys from a gas reaction point of view, J. Alloys Compd. 293 (1999) 877–888. doi:10.1016/S0925-8388(99)00384-9.

[64] E. Akiba, H. Iba, Hydrogen absorption by Laves phase related BCC solid solution, Intermetallics. 9795 (1998) 461–470. doi:10.1016/S0966-9795(97)00088-5.

[65] R. Bau, M.H. Drabnis, Structures of transition metal hydrides determined by neutron diffraction, Inorganica Chim. Acta. 259 (1997) 27–50. doi:10.1016/S0020-1693(97)89125-6.

[66] K. Edalati, R. Uehiro, Y. Ikeda, H.W. Li, H. Emami, Y. Filinchuk, M. Arita, X. Sauvage, I. Tanaka, E. Akiba, Z. Horita, Design and synthesis of a magnesium alloy

for room temperature hydrogen storage, Acta Mater. 149 (2018) 88–96. doi:10.1016/j.actamat.2018.02.033.

APPENDIX I

The heat of mixing for atomic pairs

The following table provides the binary enthalpy of mixing values given in kJ/mol calculated by Miedema's model [29]. The set of elements considering mainly elements often used in hydrogen storage applications or the study of high entropy alloys.

MgAl = -2	MgTi = +16	MgV = +23	MgCr = +21	MgMn = +10	MgFe +18	MgCo +3	MgNi = -4
AlTi = -30	AlV = -16	AlCr = -10	AlMn = -19	AlFe = -11	AlCo = -19	AlNi = -22	AlCu = -1
TiV = -2	TiCr = -7	TiMn = -8	TiFe = -17	TiCo = -28	TiNi = -35	TiCu = -9	TiZn = -15
VCr = -2	VMn = -1	VFe = -7	VCo = -14	VNi = -18	VCu = +5	VZn = -2	VZr = -4
CrMn = +2	CrFe = -1	CrCo = -4	CoNi = -7	CoCu = +12	CrZn = +5	CrZr = -12	CrNb = -7
MnFe = 0	MnCo = -5	MnNi = -8	MnCu = +4	MnZn = -6	MnZr = -15	MnNb = -4	MnMo = +5
FeCo = -1	FeNi = -2	FeCu = +13	FeZn = +4	FeZr = -25	FeNb = -16	FeMo = -2	FePd = -4
CoNi = 0	CoCu = +6	CoZn = -5	CoZr = -41	CoNb = -25	CoMo = -5	CoPd = -1	CoLa = -17
NiCu = +4	NiZn = -9	NiZr = -49	NiNb = -30	NiMo = -7	NiPd = 0	NiLa = -27	NiHf = -42
CuZn = +1	CuZr = -23	CuNb = +3	CuMo = +19	CuPd = -14	CuLa = -21	CuHf = -17	CuTa = +2
ZnZr = -29	ZnNb = -1	ZnMo = +12	ZnPd = -33	ZnLa = -31	ZnHf = -24	ZnTa = +3	ZnW = +15
ZrNb = +4	ZrMo = -6	ZrPd = -91	ZrLa = +13	ZrHf = +13	ZrTa = +3	ZrW = -9	
NbMo = -6	NbPd = -53	NbLa = +36	NbHf = +4	NbTa = 0	NbW = -8		
MoPd = -15	MoLa = +31	MoHf = -4	MoTa = -5	MoW = 0			
PdLa = -82	PdHf = -80	PdTa = -52	PdW = -6				
LaHf = +15	LaTa = +33	LaW = +32					
HfTa = +3	HfW = -6						
TaW = -7							

MgCu = -3	MgZn = -4	MgZr = +6	MgNb = +32	MgMo = +36	MgPd = -40	MgLa = -7	MgHf = +10	MgTa = +30	MgW = +38
AlZn = +1	AlZr = -44	AlNb = -18	AlMo = -5	AlPd = -46	AlLa = -38	AlHf = -39	AlTa = -19	AlW = -2	
TiZr = 0	TiNb = +2	TiMo = -4	TiPd = -65	TiLa = +20	TiHf = 0	TiTa = +1	TiW = -6		
VNb = -1	VMo = 0	VPd = -35	Vla = +22	VHf = -2	VTa = -1	VW = -1			
CrMo = 0	CrPd = -15	CrLa = +17	CrHf = -9	CrTa = -7	CrW = +1				
MnPd = -23	MnLa = +3	MnHf = -12	MnTa = -4	MnW = +6					
FeLa = +5	FeHf = -21	FeTa = -15	FeW = 0						
CoHf = -35	CoTa = -24	CoW = -1							
NiTa = -29	NiW = -3								
CuW = +22									

APPENDIX II

Elemental Properties

Properties of chemical elements. Data taken from Ye et al. [11] for a straight comparison in phi values calculated in section 5.2.

	Atomic size (Å)	Tm (K)
Li	1.519	453.69
Be	1.128	1560.00
B	0.82	2348.00
C	0.773	3823.00
N	0.75	63.05
Na	1.857	370.87
Mg	1.601	923.00
Al	1.432	933.47
Si	1.153	1687.00
P	1.06	317.30
Ca	1.976	1115.00
Sc	1.641	1814.00
Ti	1.462	1941.00
V	1.316	2183.00
Cr	1.249	2180.00
Mn	1.35	1519.00
Fe	1.241	1811.00
Co	1.251	1768.00
Ni	1.246	1728.00
Cu	1.278	1357.77
Zn	1.395	692.68
Ga	1.392	302.91
Ge	1.24	1211.40
Sr	2.152	1050.00
Y	1.802	1799.00
Zr	1.603	2128.00
Nb	1.429	2750.00
Mo	1.363	2896.00
Tc	1.36	2430.00
Rh	1.345	2237.00
Pd	1.375	1828.05

Ag	1.445	1234.93
Cd	1.568	594.22
La	1.879	1193.00
Ce	1.825	1071.00
Nd	1.64	1294.00
Eu	1.8	1095.00
Gd	1.801	1586.00
Tb	1.773	1629.00
Dy	1.781	1685.00
Er	1.761	1770.00
Yb	1.74	1092.00
Hf	1.578	2506.00
Ta	1.43	3290.00
W	1.367	3695.00
Pt	1.387	2041.40
Au	1.442	1337.33
Pb	1.75	600.61
Sn	1.62	505.08

APPENDIX III

The excess entropy of mixture

The Z compressibility for mixtures of hard spheres:

$$Z = [(1 + \xi + \xi^2) - 3\xi(y_1 + y_2\xi) - \xi^3 y_3](1 - \xi)^{-3}$$

where:

$$y_1 = \sum_{j>i=1}^{m} \Delta_{ij}(d_i + d_j)(d_i d_j)^{-\frac{1}{2}}$$

$$y_2 = \sum_{j>i=1}^{m} \Delta_{ij} \sum_{k=1}^{m} (\frac{\xi_k}{\xi}) \frac{(d_i d_j)^{\frac{1}{2}}}{d_k}$$

$$y_3 = \left[\sum_{i=1}^{m} \left(\frac{\xi_i}{\xi}\right)^{\frac{2}{3}} c_i^{\frac{1}{3}}\right]^3$$

$$\Delta_{ij} = \left[(\xi_i \xi_j)^{\frac{1}{2}}/\xi\right]\left[(d_i - d_j)^2/d_i d_j\right](c_i c_j)^{\frac{1}{2}}$$

$$\xi = \sum_{i=1}^{m} \xi_i$$

$$\xi_i = \frac{1}{6}\pi\rho d_i^3 c_i$$

where d_i is the atomic diameter of the ith element, c_i is the molar fraction of the ith element, ρ is the density number and ξ is the general atomic packaging fraction for a given ρ. The excess entropy of mixture S_E is then expressed, in terms of c_i, d_i and ξ, as follows:

$$\frac{S_E}{k_B} = \frac{(F - F^{id})}{k_B T} - \ln Z - (3 - 2\xi)(1 - \xi)^{-2} + 3 + \ln[(1 + \xi + \xi^2 - \xi^3)(1 - \xi)^{-3}]$$

Where:

$$\frac{(F - F^{id})}{k_B T} = -\frac{3}{2}(1 - y_1 + y_2 + y_3) + (3y_2 + 2y_3)(1 - \xi)^{-1} + \frac{3}{2}(1 - y_1 - y_2 - \frac{1}{3}y_3)(1 - \xi)^{-2} + (y_3 - 1)\ln(1 - \xi)$$